Available online at www.sciencedirect.com

ScienceDirect

Geochimica et Cosmochimica Acta 324 (2022) 221–239

Geochimica et Cosmochimica Acta

www.elsevier.com/locate/gca

Decoupling of chemical and isotope fractionation processes during atmospheric heating of micrometeorites

Seppe Lampe [a,*], Bastien Soens [a,b], Stepan M. Chernonozhkin [c], Claudia González de Vega [c], Matthias van Ginneken [d], Flore Van Maldeghem [a], Frank Vanhaecke [c], Billy P. Glass [e], Ian A. Franchi [f], Herman Terryn [g], Vinciane Debaille [b], Philippe Claeys [a], Steven Goderis [a]

[a] *Analytical-, Environmental-, and Geo-Chemistry (AMGC), Vrije Universiteit Brussel, Pleinlaan 2, B-1050 Brussels, Belgium*
[b] *Laboratoire G-Time, Université Libre de Bruxelles 50, Av. F.D. Roosevelt CP 160/02, B-1050 Brussels, Belgium*
[c] *Atomic & Mass Spectrometry – A&MS Research Unit, Department of Chemistry, Ghent University, Krijgslaan, 281 – S12, B-9000 Ghent, Belgium*
[d] *Centre for Astrophysics and Planetary Science, School of Physical Sciences, University of Kent, Canterbury CT2 7NZ, United Kingdom*
[e] *Department of Geological Sciences, University of Delaware, 261 S. College Ave, 111 Robinson Hall, Newark, DE 19716-1304, United States*
[f] *Planetary and Space Sciences, School of Physical Sciences, The Open University, Walton Hall, Milton Keynes MK7 6AA, United Kingdom*
[g] *Electrochemical and Surface Engineering, Vrije Universiteit Brussel, Pleinlaan 2, B-1050 Brussels, Belgium*

Received 9 April 2021; accepted in revised form 6 February 2022; Available online 11 February 2022

Abstract

Micrometeorites experience varying degrees of evaporation and mixing with atmospheric oxygen during atmospheric entry. Evaporation due to gas drag heating alters the physicochemical properties of fully melted cosmic spherules (CSs), including the size, chemical and isotopic compositions and is thus expressed in its chemical and isotopic signatures. However, the extent of evaporation and atmospheric mixing in CSs often remains unclear, leading to uncertainties in precursor body identification and statistics. Several studies have previously estimated the extent of evaporation based on the contents of major refractory elements Ca and Al in combination with the determined Fe/Si atomic ratios. Similarly, attempts have been made to design classification schemes based on isotopic variations. However, a full integration of any previously defined chemical classification schemes with the observed isotopic variability has not yet been successful. As evaporation can lead to both chemical and isotope fractionation, it is important to verify whether the estimated degrees of evaporation based on chemical and isotopic proxies converge. Here, we have analysed the major and trace element compositions of 57 chondritic (mostly V-type) CSs, along with their Fe isotope ratios. The chemical (Zn, Na, K or CaO and Al_2O_3 concentrations) and δ^{56}Fe isotope fractionation measured in these particles show no correlation. The interpretation of these results is twofold: (i) isotopic and chemical fractionation are governed by distinct processes or (ii) the proxies selected for chemical and isotope fractionation are inadequate. While the initial Fe isotopic ratios of chondrites are constrained within a relatively narrow range (0.005 ± 0.008‰ δ^{56}Fe), the chemical compositions of CSs display larger variability. Cosmic spherules are thus often not chemically representative of their precursor bodies, due to their small size. As oxygen isotopes are commonly used to refine the precursor bodies of meteorites, triple oxygen isotope ratios were measured in thirty-seven of the characterized CSs. Based on the relationship between δ^{18}O and δ^{57}Fe, the evaporation effect on the O isotope system can be calculated, which allows for a more accurate parent body determination. Using this correction method, two 'Group 4' spherules with strongly variable

* Corresponding author.
E-mail address: seppe.lampe@vub.be (S. Lampe).

https://doi.org/10.1016/j.gca.2022.02.008
0016-7037/© 2022 Elsevier Ltd. All rights reserved.

degrees of isotope fractionation (δ^{56}Fe of ~1.0‰ and 29.1‰, respectively) could be distinguished. Furthermore, it was observed that all CSs that probably have a OC-like heritage underwent roughly the same degree of atmospheric mixing (~8‰ δ^{18}O). This highlights the potential of including Fe isotope measurements to the regular methodologies applied to CS studies.
© 2022 Elsevier Ltd. All rights reserved.

Keywords: Cosmic spherules; Atmospheric entry heating; Iron isotope ratios; Isotope fractionation; Precursor bodies

1. INTRODUCTION

Annually ~40 000 tonnes of extraterrestrial material accumulates on the Earth, predominantly in the form of micrometeorites (Love and Brownlee, 1993; Plane et al., 2018; Zolensky et al., 2006). Micrometeorites are extraterrestrial particles in the size range of 10–2000 μm that (partially) survived their transit through the atmosphere (Rubin and Grossman, 2010). Their precursors stem from the proximate interplanetary dust cloud, which is mostly composed of asteroidal particles from the Main Asteroid Belt and material from the Jupiter Family Comets (Dermott et al., 1991; Flynn, 1992; Nesvorný et al., 2010; Rojas et al., 2021). These particles are transported to Earth through Poynting-Robertson drag and some of them originate from source reservoirs different from those of macroscopic meteorites (Wyatt and Whipple, 1950; Dermott et al., 1991; Flynn, 1992; Kral et al., 2017). Classifications based on oxygen isotope ratios show that at least 60% of all micrometeorites in all size fractions are related to more primitive objects, displaying carbonaceous chondritic compositions (Engrand et al., 1999; Yada et al., 2005; Suavet et al., 2010). Another ~20% of the micrometeoroid complex is fed by evolved asteroids common in the inner asteroid belt, i.e., the ordinary chondrite parent bodies and, subordinately, the howardite-eucrite-diogenite (HED) parent asteroid(s) (Cordier and Folco, 2014). However, these parent body contributions are highly size-dependent, with the relative proportion of ordinary chondrite material in the micrometeorite complex increasing with micrometeorite size and at 250–500 μm the OC/CC ratio approximating 1 (Cordier and Folco, 2014; Goderis et al., 2020). Likely, a continuous relationship exists between the contributions of precursor materials of micrometeorites and macroscopic meteorites, where smaller particles are more often derived from (brittle) carbonaceous chondrites (Flynn et al., 2009; Goderis et al., 2020).

Upon entering the Earth's atmosphere, micrometeorites decelerate in a few seconds from velocities of kilometres per second to centimetres per second (Toppani et al., 2001; Genge et al., 2008). Deceleration causes melting and evaporation by pulse heating of the incoming particle, which effectively modify the original texture, chemical composition and isotopic ratios of the micrometeoroids. Particle size, velocity, precursor chemistry, density and entry angle determine the extent of thermal alteration of the micrometeorite during its atmospheric entry (Love and Brownlee, 1991). With a more limited particle size and density, a low entry angle (~horizontal) and low velocity, primary characteristics of the incoming particle are more likely to be preserved (Flynn, 1992; Love and Brownlee, 1993). Consequently, the most pristine micrometeorites are often recovered from the smallest size fractions. Cosmic spherules represent those micrometeorites that have completely melted and principally display round morphologies (Genge et al., 2008). These particles have often lost their initial textures and a substantial amount of their volatile element contents due to evaporation (e.g., Zn, Na, K; Flynn and Sutton, 1992; Presper et al., 1993; Greshake et al., 1998; Cordier et al., 2011a). Compared to these volatile elements, the isotopic ratios of more refractory elements such as Fe, Si, and Mg also display significant degrees of isotope fractionation (Alexander et al., 2002; Taylor et al., 2005; Engrand et al., 2005; Yada et al., 2005). Among CSs, silicate-rich (S-type) CSs are the most abundant form, constituting 97% of CSs in collections representative of the flux of micrometeorites to Earth (Taylor et al., 2000; Genge et al., 2008; Rochette et al., 2008; Goderis et al., 2020). According to their quench textures, S-type cosmic spherules are further subdivided into the porphyritic olivine (PO-type), micro-porphyritic olivine, barred olivine (BO-type), cryptocrystalline (CC-type), vitreous (V-type) and Ca-Al-Ti (CAT) subtypes, reflecting increasingly higher peak temperatures (Taylor and Brownlee, 1991; Taylor et al., 2000; Genge et al., 2008; van Ginneken et al., 2017).

Generally considered homogeneous (Genge, 2008), V-type CSs have additionally been divided into three chemical subgroups (Cordier et al., 2011a). The 'normal chondritic' spherules, 'CAT-like' spherules and 'high Ca-Al' spherules display a progressive enrichment in the concentrations of the refractory major element oxides (including CaO, Al_2O_3 and TiO_2) and refractory trace elements (e.g., Zr and REE; Alexander et al., 2002; Cordier et al., 2011a; Goderis et al., 2020). The gradual enrichment in refractory components relative to volatile and moderately refractory elements in these subgroups has been interpreted to reflect discrete degrees of evaporation and/or separation of high-density phases (e.g., metallic Fe-Ni and sulphide beads, spinel group minerals) during atmospheric entry (Cordier et al., 2011a; Goderis et al., 2020). Due to these processes, CSs lost approximately 40–90% of their initial mass during atmospheric entry (Love and Brownlee, 1991; Cordier et al., 2011a). Rounded Fe-Ni beads are formed from immiscible Fe-rich liquids during the melting of CSs. Due to the centrifugal forces in the spinning spherules, these liquids are transported to the outer sides where they can be ejected (Genge and Grady, 1998). Volatile elements such as K, Na and S are lost significantly, while moderately refractory elements such as Fe, Si, Mg, Ni and Cr display distinct evaporation rates (Alexander et al.,

2002; Engrand et al., 2005). In addition to changes in element concentrations, evaporation can also be traced by a mass-dependent shift of isotope ratios towards heavier values, as previously demonstrated for example for O, Fe, Si, Mg, Ni and Cr (Alexander et al., 2002; Taylor et al., 2005; Engrand et al., 2005; González de Vega et al., 2020a, 2020b).

Extraterrestrial materials are often classified based on their oxygen isotope ratios, as various Solar System and planetary reservoirs display distinct non-mass dependent values of $\delta^{16}O$, $\delta^{17}O$ and $\delta^{18}O$, inherited from the nebular stage. In the case of CSs, the oxygen isotope ratios ($^{17}O/^{16}O$ and $^{18}O/^{16}O$) are commonly modified during atmospheric entry through mass-dependent fractionation and mixing with atmospheric oxygen (Clayton et al., 1976; Herzog et al., 1999; Engrand et al., 2005; Taylor et al., 2005; Yada et al., 2005; Suavet et al., 2010; Cordier et al., 2011b; Rudraswami et al., 2012; van Ginneken et al., 2017). After a particle is quenched and deposited in a sedimentary trap, its oxygen isotope ratios can additionally be modified by alteration processes under Antarctic weathering conditions (Goderis et al., 2020). Despite the isotopic shifts linked to these processes, the oxygen isotope ratios of CSs often enable assignment to a particular parent body or meteorite group (e.g., Suavet et al., 2010; Rudraswami et al., 2012; van Ginneken et al., 2017; Goderis et al., 2020).

Chondritic meteorites, considered the precursor materials for the majority of micrometeorites, display a narrow $\delta^{56}Fe$ isotope range of 0.005 ± 0.008‰ (n = 42; Craddock et al., 2013; Barrat et al., 2015; Chernonozhkin et al., 2016). While the ejection of Fe-Ni beads lowers the Fe content of a CS, this process does not significantly influence the isotopic composition of Fe, as metal-silicate isotope fractionation at high temperature is assumed to be generally limited (Taylor et al., 2005). In contrast, evaporation during atmospheric passage not only lowers the Fe-content of the precursor but also shifts the Fe isotope ratios to heavier values following a mass-dependent relation

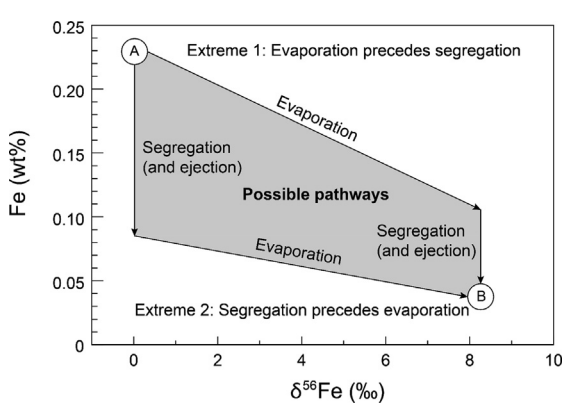

Fig. 1. The effects of evaporation and metal bead segregation (and ejection) on the Fe content and $\delta^{56}Fe$ of a CS. Note that the two extreme pathways result in varying amounts of evaporation and metal bead segregation, yet still end up at the same Fe content and $\delta^{56}Fe$. This complicates estimating evaporation based on $\delta^{56}Fe$ only. Modified after Taylor et al. (2005).

(Fig. 1). Advances in mass spectrometry over the last few decades allow limited sample sizes to be analyzed at relatively high-precision (~0.05‰ for $\delta^{56}Fe$; 2SD).

This work aims to better constrain the chemical and isotope fractionation processes that take place during the melting and evaporation of micrometeorites and the precursor materials from which these particles derive. Although complemented by bulk data for CSs of most textural groups, the focus here is placed on vitreous CSs because of the absence of potential mineral-dependent analytical artefacts on these CSs, and also because V-type particles experienced high peak temperatures, which amplifies possible mass-dependent isotope fractionation effects.

2. MATERIALS AND METHODS

All but one (particle number 188-5) of the samples analysed during this study were extracted from the Widerøefjellet 2B deposit collected during the 2012–2013 MICROMETA expedition in the Sør Rondane Mountains in Antarctica. The extraction procedure for micrometeorites is described in detail in Goderis et al. (2020). A series of relatively fresh chondritic CSs was selected based on Secondary Electron Microscope Energy-Dispersive X-ray Spectroscopy (SEM-EDS) images and data, acquired using the JEOL JSM IT-300 instrument of the SURF research group at the Vrije Universiteit Brussel (VUB; Fig. 2). Each CS was categorised according to the weathering scale described in van Ginneken et al. (2016) (Supplementary Table EA1). Cosmic spherule 188-5, roughly 200 µm in diameter, was collected within marine sediments during an oceanographic expedition in the Indian Ocean southwest of Australia, at location RC8-52 (41.10S 101.42E). The selected micrometeorites were embedded in three epoxy mounts, one ("Mount 1") containing thirteen V-type CSs (WF1202B-0001 up to WF1202B-0048) in the size range of 478–828 µm, a second ("Mount 2") holding another twenty-four vitreous CSs (WF1202B-0201 to WF1202B-0224) with a diameter between 208 and 348 µm, and a third ("Mount 3") with nineteen spherules of various textural groups with a diameter of 129–637 µm. Mount 3 contains three PO-type spherules (WF1202B-0226, WF1202B-0227 and WF1202B-0228), four BO-type (WF1202B-0229 – WF1202B-0232) and CC-type spherules (WF1202B-0233 – WF1202B-0236), six V-type CSs (WF1202B-0237 – WF1202B-0242), a single white BO-type (WF1202B-0243) and one scoriaceous micrometeorite (WF1202B-0244). The white BO-type CS has a milky-white appearance and barred olivine texture but lacks the typical high Mg/Si ratio and high Ca, Al and Ti values associated with white barred olivine CAT CSs (Genge et al., 2008). Supplementary Table EA1 contains an overview of the measuring techniques that are applied on each CS. The major element concentrations for the particles in Mount 1 have previously been measured relying on a combination of electron microprobe analysis (EMPA) and laser ablation inductively coupled plasma mass spectrometry (LA-ICP-MS), while the trace elements have been measured solely with LA-ICP-MS, both are reported in Goderis et al. (2020). The major and trace element concentrations for particles in Mount 2

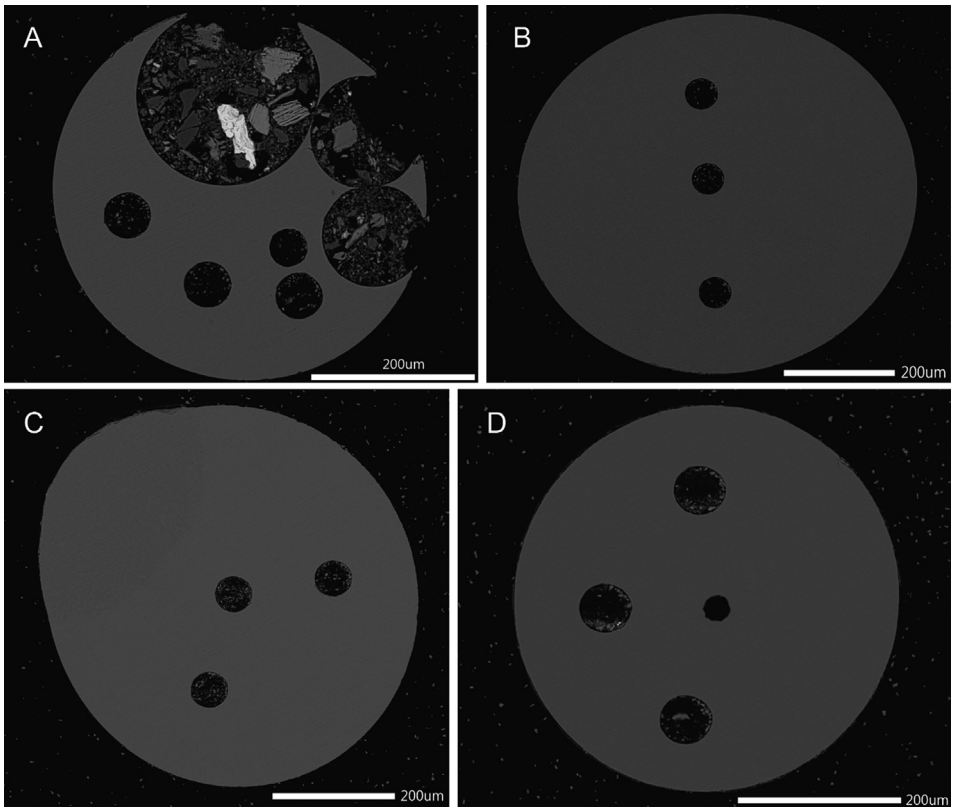

Fig. 2. SEM images (BSE) of four CSs, from left to right and top to bottom, WF1202B-0004, WF1202B-0009, WF1202B-0024 and WF1202B-0048. The black holes are remnants from the LA-ICP-MS measurements, while the three larger circular structures in the left upper image are vesicles. The spherules do not display evidence for extensive terrestrial weathering. The smaller dark sphere in the centre of (d) is likely linked to contamination of the particle mount after analysis.

and 3 were determined using a Teledyne Cetac Analyte G2 laser ablation system in combination with a Thermo Scientific Element XR inductively coupled plasma mass-spectrometer at Ghent University, following the procedure outlined in Chernonozhkin et al. (2021). Following this procedure, precise and accurate major, minor and trace element concentrations were obtained for USGS glass reference materials BCR-2G and BIR-1G. The average bias between reference value and experimentally obtained value is typically <10%. Based on the analyses of the reference materials, the reproducibility for the elements measured is 5–10% relative standard deviation (RSD), depending on the concentration.

The oxygen isotope ratios of the particles in Mount 1 were analysed using a NanoSIMS 50L instrument at the Open University (Milton Keynes, UK) according to the procedure outlined in Starkey and Franchi (2013). A Cs^+ primary ion beam (~25 pA) was rastered over a 5 μm square to produce $^{16}O^-$, $^{17}O^-$, and $^{18}O^-$ ions from each sample. The signal intensity for ^{16}O was measured using a Faraday Cup (FC), while electron multipliers were used to determine the count rates for the $^{17}O^-$, $^{18}O^-$ and $^{24}Mg^{16}O^-$ ions. Each micrometeorite was measured in between 2 and 6 times, and San Carlos olivine was used as reference material. The oxygen isotope ratios of the CSs in Mount 2 were measured using a CAMECA IMS 1270 E7 SIMS at the Centre de Recherches Pétrographiques et Géochimiques (CRPG-CNRS; Nancy, France). For the SIMS measurements, the count rates for $^{16}O^-$, $^{17}O^-$, and $^{18}O^-$ ions produced by a Cs^+ primary ion beam (~15 μm, ~2.5 nA) were determined in multi-collection mode using two off-axis FCs for $^{16}O^-$ and $^{18}O^-$ and the axial FC for $^{17}O^-$. Mass resolution was set at ~10,000 (Cameca definition) to resolve ^{17}O from ^{16}OH. Instrumental fractionation was corrected by calibration against San Carlos olivine measured alongside the samples. To resolve the $^{16}OH^-$ interference on the $^{17}O^-$ peak and to obtain maximum flatness on the top of the $^{16}O^-$ and $^{18}O^-$ peaks, entrance and exit slits were adjusted to acquire a spectral resolution of ≈7000 for $^{17}O^-$ on the central FC. The multicollection FCs were set on slit 1 (MRP = 2500). Each micrometeorite was measured three times and each measurement consisted of 275 seconds, including 90 s pre-sputtering. At CRPG Nancy, three in-house terrestrial standard materials (San Carlos olivine, CLDR01 MORB glass and JV1 diopside) were used to: (i) define the instrumental mass fractionation line for the 3 oxygen isotopes, and (ii) correct the instrumental mass fractionation (IMF) due to the matrix effect in samples. Based on the repeated analyses of the terrestrial reference materials (San Carlos olivine, CLDR01 MORB glass, and/or BURMA spinel) and measured samples, the 2SD expanded uncertainties

$\left(2 * \sqrt{SE_{ref}^2 + SE_{sample}^2}\right)$, with SE being the standard error) were calculated to be ~0.5‰ for $\delta^{17}O$, ~0.5‰ for $\delta^{18}O$, and ~0.6‰ for $\Delta^{17}O$ during the SIMS session (with $\Delta^{17}O$ representing the deviation from the TFL, $\Delta^{17}O = \delta^{17}O - 0.52 \times \delta^{18}O$; Clayton, 1993). Note that the repeatability, expressed as 2 standard deviations based on repeated measurements of the same cosmic spherule (typically $N = 3$ in the SIMS session), is in some particles considerably larger (Table 1), suggesting incomplete homogenisation, potential effects from minor (Antarctic) alteration, or contribution of an additional unknown source of measurement uncertainty. Larger 2SD uncertainties of ~1.6‰ for $\delta^{17}O$, ~0.9‰ for $\delta^{18}O$, and ~1.7‰ for $\Delta^{17}O$ were obtained for the NanoSIMS session, yet the repeatability (2SD on the repeated measurements, with $N = 2$–6) is often comparable ($\Delta^{17}O$) or better ($\delta^{18}O$) than that obtained for this SIMS session.

In-situ Fe isotope ratio measurements of the micrometeorites were performed using a ns-LA-MC-ICP-MS set-up combining an Analyte G2 193 nm ArF*excimer-based LA-system (Teledyne Photon Machines Inc., Bozeman, MT, USA), equipped with a COBALT ablation cell and ARIS aerosol rapid introduction system (PEEK tubing with 1 mm ø; Van Malderen et al., 2020), with a Thermo Scientific Neptune MC-ICP-MS instrument equipped with high-transmission interface and a Pfeiffer (Germany) OnTool™ Booster 150 dry interface pump (130 m^3 h^{-1} pumping speed) at Ghent University (Ghent, Belgium). Instrumental mass discrimination correction relied on internal doping with a standard solution of Ni (500 ng mL^{-1}), continuously aspirated via pneumatic nebulizer and a double pass spray chamber, using a T-piece (5 mm ø) for mixing. The Fe isotope ratios were additionally corrected for potential drift by sample-standard bracketing using the United States Geological Survey (USGS) basaltic glass reference material BCR-2G. The BCR-2G reference glass was ablated using a circular spot size of 15 μm diameter, laser energy density of 1.74 J cm^{-2} and a laser repetition rate of 20 Hz. To assure for an adequate correction relative to the reference material, the Fe intensities for the cosmic spherules were matched within 5% to those obtained for BCR-2G by adjusting the spot size (10–30 μm) and laser repetition rates (25–45 Hz). Nuclides ^{53}Cr, ^{54}Fe, ^{56}Fe, ^{57}Fe, ^{58}Ni and ^{60}Ni were measured simultaneously in an array of six Faraday cups at medium mass resolution ($m/\Delta m \sim 6000$). ^{53}Cr was monitored to correct for the potential isobaric interference of ^{54}Cr on ^{54}Fe, applying the natural abundances of Cr. Further details of the method can be found in González de Vega et al. (2020a). In addition, a set of nineteen CSs of different textural and chemical groups were digested in their entirety after LA-ICP-MS for major and trace element characterization. The pure Fe fractions were separated from matrix using anion exchange chromatography and the Fe isotopic compositions were measured using wet pneumatic nebulization (PN-)MC-ICP-MS. The Fe isotope ratios of the CSs are expressed as δ-values relative to IRMM-014 international reference material, with reference material, with $\delta^{ii}Fe = [(^{i}Fe/^{54}Fe)_{sample}/(^{i}Fe/^{54}Fe)_{reference\ material} - 1] \cdot 1000‰$ (González de Vega et al., 2020b). Here ^{i}Fe represents the isotopes of interest i = 56, 57. Based on fifteen ns-LA-MC-ICP-MS measurements in multiple analytical sessions of BCR-2G reference material, the intermediate precision (2SD) is ~0.10‰ and ~0.14‰ for $\delta^{56}Fe$ and $\delta^{57}Fe$, respectively. Similarly, based on four measurement sessions that included seven reference materials, the intermediate precision (2SD) for the PN-MC-ICP-MS is ~0.05‰ and ~0.07‰ for $\delta^{56}Fe$ and $\delta^{57}Fe$, respectively (González de Vega et al., 2020b).

3. RESULTS

For the purpose of this study, only chondritic particles were selected based on their distribution in Fe/Mn versus Fe/Mg space (Fig. 3a). This classification is supported by trends observed for CaO + Al_2O_3 versus Fe/Si, and Si/Al versus Mg/Al (Fig. 4), as well as the measured REE patterns (Supplementary Fig. EA1; Goodrich and Delaney, 2000; Taylor et al., 2005; Taylor et al., 2007; Cordier et al., 2011a). The CaO + Al_2O_3 vs. Fe/Si plot can be used to subdivide V-type CSs in chemical subtypes (Table 1; Cordier et al., 2011a), as the concentrations of refractory major element oxides CaO and Al_2O_3 are appropriate parameters to study the degree of evaporation due to their relatively high condensation temperatures of ca. 50% T_C = 1517 K (Ca) and 1653 K (Al; Lodders, 2003). Thirty-nine of the forty-four V-type CSs, along with the three POs, four BOs and CCs and the one scoriaceous spherule, are classified here as part of the normal chondritic subgroup, according to the classification of Cordier et al. (2011a). Spherules WF1202B-0010 and 0048 are the only V-types with Fe/Si < 0.06 and CaO + Al_2O_3 > 5 wt%, and can thus be designated as 'CAT-like' spherules, although both lack a typical milky-white appearance, as described by Cordier et al. (2011a). In contrast, the white BO-type particle (WF1202B-0243), also classified as 'CAT-like', does display such characteristics. Spherules WF1202B-0001, 0020 and 0217 are classified as 'high Ca-Al' spherules (Fe/Si > 0.06 and CaO + Al_2O_3 > 9 wt%). However, two of these, WF1202B-0020 and 0217, plot near the boundary between the 'high Ca-Al' and 'normal chondritic' fields (9 wt% CaO + Al_2O_3). Spherules WF1202B-0001 and 0217 both display a pale green colour typical of the 'high Ca-Al' subgroup, while WF1202B-0020 is black. Colourless and completely transparent spherule WF1202B-0218 lies close to the triple-junction of the three respective fields but is consistent with a 'normal chondritic' classification. Particle WF1202B-0223, which is part of the 'normal chondritic' group, plots close to the 'normal chondritic'/'high Ca-Al' margin and exhibits intermediate characteristics, such as a pale green colour (Supplementary Table EA3).

The $\delta^{17}O$ results for all analysed particles range from 0.0‰ to 34.8‰, while the $\delta^{18}O$ values vary between 5.9‰ and 64.2‰ and $\Delta^{17}O$ values between −5.0‰ and +1.8‰. In Fig. 5a, $\Delta^{17}O$ values are plotted against their corresponding $\delta^{18}O$ values for all measured spherules, while the oxygen isotopic dataset is summarized in Table 1. Two CSs plot above the TFL, fourteen fall below, while

Table 1
The O and Fe isotope ratios of the CSs mentioned in this work, along with their textural and chemical subdivision. The $\delta^{18}O_{Corr}$ and $\Delta^{17}O$ were used to derive the precursor bodies of the CSs. Parent body assignments with a hyphen (e.g., 'OC-EC') cannot be assigned to one class within the 95% confidence interval. 'OC-EC' indicates that the particle likely is an OC but it cannot be excluded that the particle has an EC-heritage.

Sample name	$\delta^{18}O \pm 2SE$ (2SD) (‰)	N	$\delta^{18}O_{Corr}$ (‰)	$\Delta^{17}O \pm 2SE$ (2SD) (‰)	$\delta^{56}Fe \pm 2SE$ (‰)	$\delta^{57}Fe \pm 2SE$ (‰)	Chemical subtype	Parent body	Textural subtype
WF1202B-0001	9.0 ± 0.9 (0.2)	2	7.9	1.7 ± 1.7 (0.4)	1.23 ± 0.20	1.59 ± 0.18	High Ca-Al	Amb.	V
WF1202B-0004	10.8 ± 0.7 (1.8)	5	10.5	−0.1 ± 1.7 (1.4)	0.29 ± 0.06	0.43 ± 0.10	Normal	Amb.	V
WF1202B-0005	32.9 ± 1.0 (2.0)	3	7.0	−1.9 ± 2.0 (1.0)	24.99 ± 0.32	37.11 ± 0.29	Normal	CC-EC	V
WF1202B-0009	13.2 ± 0.7 (1.0)	5	8.21	−2.3 ± 1.7 (1.2)	4.76 ± 0.34	7.08 ± 0.14	Normal	CC	V
WF1202B-0010	6.1 ± 1.2 (1.0)	5	0.71	−3.1 ± 1.9 (1.4)	5.13 ± 0.10	7.67 ± 0.13	CAT-like	CC	V
WF1202B-0012	17.3 ± 0.7 (0.8)	5	13.3	0.1 ± 1.3 (1.4)	3.92 ± 0.10	5.61 ± 0.07	Normal	Amb.	V
WF1202B-0017	17.6 ± 0.9 (0.8)	2	13.9	−0.8 ± 1.7 (1.2)	3.56 ± 0.22	5.24 ± 0.33	Normal	Amb.	V
WF1202B-0019	23.6 ± 1.1 (1.6)	5	10.4	−0.9 ± 1.6 (1.2)	12.82 ± 0.06	18.88 ± 0.18	Normal	Amb.	V
WF1202B-0020	24.0 ± 1.1 (0.6)	6	9.2	−1.7 ± 1.6 (1.8)	14.16 ± 0.16	21.16 ± 0.23	High Ca-Al	CC-EC	V
WF1202B-0021	14.7 ± 0.9 (0.8)	3	14.5	1.8 ± 1.7 (0.2)	0.25 ± 0.16	0.38 ± 0.17	Normal	Amb.	V
WF1202B-0024	n.a.	n.a.	n.a.	n.a.	3.16 ± 0.18	4.87 ± 0.23	Normal	n.a.	V
WF1202B-0039	13.7 ± 0.7 (1.0)	5	12.7	−0.6 ± 1.3 (1.8)	0.93 ± 0.08	1.35 ± 0.08	Normal	Amb.	V
WF1202B-0048	15.1 ± 0.7 (0.8)	5	−2.0	−3.9 ± 1.4 (1.0)	16.38 ± 0.24	24.48 ± 0.22	CAT-like	CC	V
WF1202B-0201	16.9 ± 0.5 (4.7)	3	13.4	0.4 ± 0.5 (1.0)	3.38 ± 0.26	5.02 ± 0.15	Normal	OC-EC	V
WF1202B-0202	23.5 ± 0.5 (13.5)	3	20.5	−0.6 ± 0.6 (1.2)	2.88 ± 0.19	4.28 ± 0.17	Normal	CC-EC	V
WF1202B-0203	13.7 ± 0.5 (3.4)	3	11.7	−1.7 ± 0.6 (0.4)	1.87 ± 0.19	2.85 ± 0.17	Normal	CC	V
WF1202B-0204	21.0 ± 0.5 (3.1)	3	19.0	0.6 ± 0.6 (0.4)	1.83 ± 0.17	2.83 ± 0.17	Normal	OC-EC	V
WF1202B-0205	6.5 ± 0.5 (1.6)	3	6.3	0.3 ± 0.6 (1.3)	0.17 ± 0.23	0.31 ± 0.13	Normal	EC-OC	V
WF1202B-0206	21.9 ± 0.5 (6.2)	3	17.3	−1.2 ± 0.6 (0.9)	4.29 ± 0.17	6.56 ± 0.15	Normal	CC	V
WF1202B-0207	64.2 ± 0.5 (0.8)	3	34.0	1.4 ± 0.6 (0.8)	29.14 ± 0.27	43.23 ± 0.22	Normal	Gr. 4	V
WF1202B-0208	5.9 ± 0.5 (1.6)	3	1.7	−3.1 ± 0.7 (0.4)	3.87 ± 0.16	6.04 ± 0.16	Normal	CC	V
WF1202B-0209	21.9 ± 0.5 (10.6)	3	18.4	−4.1 ± 0.7 (0.7)	3.24 ± 0.23	4.95 ± 0.18	Normal	CM/CO/CV	V
WF1202B-0210	13.5 ± 0.5 (6.0)	3	12.8	0.6 ± 0.6 (0.7)	0.62 ± 0.15	1.04 ± 0.14	Normal	OC-EC	V
WF1202B-0211	22.6 ± 0.5 (9.1)	3	5.8	0.3 ± 0.6 (0.6)	16.01 ± 0.26	24.15 ± 0.19	Normal	EC-OC	V
WF1202B-0212	41.0 ± 0.5 (7.7)	3	2.1	−1.4 ± 0.6 (0.5)	37.01 ± 0.36	55.68 ± 0.31	Normal	CC (CR)	V
WF1202B-0213	12.5 ± 0.5 (3.0)	3	10.8	0.9 ± 0.7 (0.0)	1.62 ± 0.24	2.39 ± 0.11	Normal	OC-EC	V
WF1202B-0214	20.4 ± 0.5 (3.8)	3	13.6	0.4 ± 0.6 (0.4)	6.49 ± 0.18	9.82 ± 0.21	Normal	Amb.	V
WF1202B-0215	23.1 ± 0.5 (4.3)	3	7.8	−2.9 ± 0.7 (0.7)	14.51 ± 0.23	21.88 ± 0.24	Normal	CC	V
WF1202B-0216	17.2 ± 0.5 (1.1)	3	12.9	1.0 ± 0.6 (0.9)	3.96 ± 0.13	6.11 ± 0.20	Normal	OC-EC	V
WF1202B-0217	10.3 ± 0.5 (4.1)	3	9.0	−2.2 ± 0.6 (0.4)	1.25 ± 0.18	1.89 ± 0.14	High Ca-Al	CC	V
WF1202B-0218	8.6 ± 0.5 (2.2)	3	4.8	−1.1 ± 0.6 (0.6)	3.81 ± 0.32	5.40 ± 0.15	Normal	CR/CM	V
WF1202B-0219	14.9 ± 0.5 (3.7)	3	12.2	−1.3 ± 0.6 (0.5)	2.64 ± 0.19	3.93 ± 0.07	Normal	CC	V
WF1202B-0220	39.5 ± 0.5 (2.3)	3	38.4	1.3 ± 0.6 (1.0)	1.02 ± 0.2	1.61 ± 0.12	Normal	Gr. 4	V
WF1202B-0221	17.8 ± 0.5 (3.0)	3	7.6	−5.0 ± 0.6 (0.9)	9.45 ± 0.15	14.57 ± 0.22	Normal	CM/CO/CV	V
WF1202B-0222	14.1 ± 0.5 (4.2)	3	10.4	−0.8 ± 0.7 (0.3)	3.52 ± 0.23	5.34 ± 0.19	Normal	CR/CM	V
WF1202B-0223	38.2 ± 0.5 (1.4)	3	33.6	−0.5 ± 0.5 (0.9)	4.31 ± 0.19	6.54 ± 0.20	Normal	Amb.	V
WF1202B-0224	15.0 ± 0.5 (6.6)	3	13.3	0.9 ± 0.6 (0.3)	1.56 ± 0.14	2.38 ± 0.14	Normal	OC-EC	V
WF1202B-0226	n.a.	n.a.	n.a.	n.a.	0.10 ± 0.06	0.17 ± 0.10	Normal	n.a.	PO
WF1202B-0227	n.a.	n.a.	n.a.	n.a.	−0.05 ± 0.04	−0.08 ± 0.02	Normal	n.a.	PO
WF1202B-0228	n.a.	n.a.	n.a.	n.a.	0.82 ± 0.04	1.20 ± 0.06	Normal	n.a.	PO

Table 1 (*continued*)

Sample name	$\delta^{18}O \pm 2SE$ (2SD) (‰)	N	$\delta^{18}O_{Corr}$ (‰)	$\Delta^{17}O \pm 2SE$ (2SD) (‰)	$\delta^{56}Fe \pm 2SE$ (‰)	$\delta^{57}Fe \pm 2SE$ (‰)	Chemical subtype	Parent body	Textural subtype
WF1202B-0229	n.a.	n.a.	n.a.	n.a.	0.85 ± 0.07	1.29 ± 0.17	Normal	n.a.	BO
WF1202B-0230	n.a.	n.a.	n.a.	n.a.	0.47 ± 0.04	0.68 ± 0.02	Normal	n.a.	BO
WF1202B-0231	n.a.	n.a.	n.a.	n.a.	0.73 ± 0.06	1.19 ± 0.05	Normal	n.a.	BO
WF1202B-0232	n.a.	n.a.	n.a.	n.a.	1.14 ± 0.01	1.72 ± 0.04	Normal	n.a.	BO
WF1202B-0233	n.a.	n.a.	n.a.	n.a.	0.22 ± 0.14	0.30 ± 0.10	Normal	n.a.	CC
WF1202B-0234	n.a.	n.a.	n.a.	n.a.	−0.04 ± 0.04	−0.07 ± 0.04	Normal	n.a.	CC
WF1202B-0235	n.a.	n.a.	n.a.	n.a.	0.16 ± 0.07	0.25 ± 0.10	Normal	n.a.	CC
WF1202B-0236	n.a.	n.a.	n.a.	n.a.	3.52 ± 0.04	5.45 ± 0.05	Normal	n.a.	CC
WF1202B-0237	n.a.	n.a.	n.a.	n.a.	2.06 ± 0.02	3.06 ± 0.06	Normal	n.a.	V
WF1202B-0238	n.a.	n.a.	n.a.	n.a.	1.66 ± 0.05	2.46 ± 0.02	Normal	n.a.	V
WF1202B-0239	n.a.	n.a.	n.a.	n.a.	2.46 ± 0.08	3.88 ± 0.16	Normal	n.a.	V
WF1202B-0240	n.a.	n.a.	n.a.	n.a.	4.13 ± 0.08	6.17 ± 0.01	Normal	n.a.	V
WF1202B-0241	n.a.	n.a.	n.a.	n.a.	3.61 ± 0.01	5.65 ± 0.10	Normal	n.a.	V
WF1202B-0242	n.a.	n.a.	n.a.	n.a.	4.10 ± 0.09	6.10 ± 0.08	Normal	n.a.	V
WF1202B-0243	n.a.	n.a.	n.a.	n.a.	11.14 ± 0.05	16.88 ± 0.02	CAT-like	n.a.	White BO
WF1202B-0244	n.a.	n.a.	n.a.	n.a.	0.04 ± 0.06	0.06 ± 0.04	Normal	n.a.	Scor.
188-5	n.a.	n.a.	n.a.	n.a.	21.74 ± 0.16	32.52 ± 0.27	Normal	n.a.	V

twenty are ambiguous. Ambiguous CSs are those that cannot be assigned to a specific precursor body type within 95% confidence interval. The results of Fe isotope ratio measurements in 57 cosmic spherules using both the ns-LA-MC-ICP-MS and the PN-MC-ICP-MS set-ups (−0.05 ± 0.04‰ up to 37.01 ± 0.36‰ δ^{56}Fe, 2SD) greatly exceed the natural Fe isotope fractionations in chondrites (0.005 ± 0.008‰ δ^{56}Fe), and are presented in Table 1 and displayed in Fig. 6 (Craddock et al., 2013). The δ^{56}Fe and δ^{57}Fe values fall near the terrestrial fractionation line within uncertainty, and no non-mass-dependent or nucleosynthetic isotopic effects can be resolved. The δ^{56}Fe ± 2SE values range from −0.05 ± 0.04‰ to 37.01 ± 0.36‰ and δ^{57}-Fe ± 2SE values vary between 0.31 ± 0.13‰ and 55.68 ± 0.31‰ for vitreous CSs measured by LA-MC-ICP-MS. The data for the single scoriaceous micrometeorite overlap with the values compiled for chondrites, with 0.04 ± 0.06‰ for δ^{56}Fe and 0.06 ± 0.04‰ for δ^{57}Fe (2SD; Table 1). From PO-type (−0.05 ± 0.04‰ to 0.82 ± 0.04‰, 2SD), BO-type (0.47 ± 0.04‰ to 1.14 ± 0.01‰, 2SD), CC-type (−0.04 ± 0.04‰ to 3.52 ± 0.04‰, 2SD), to V-type CSs (0.17 ± 0.22‰ to 37.01 ± 0.36‰, 2SD), the mean δ^{56}Fe values increase in line with the increasing peak temperatures suggested for these textural groups (e.g., Taylor et al., 2000). The single white barred olivine CS included in this work has a δ^{56}Fe of 11.14 ± 0.05‰ and δ^{57}Fe of 16.88 ± 0.02‰ (2SD).

4. DISCUSSION

4.1. Chemical signatures and classification

To confirm the chondritic nature of the CSs studied, first the atomic ratios of Fe/Mn and Fe/Mg are compared (Goodrich and Delaney, 2000). Originally used to characterize macroscopic meteorites, this approach can be extended to micrometeorites as well, following a few minor considerations (Taylor et al., 2007). Due to their small size, mineralogical biases can cause the initial Fe/Mn and Fe/Mg ratios of CSs to differ from the ratios of their bulk parent bodies. Additionally, evaporation and the ejection of Fe-Ni metal beads can (slightly) alter the initial Fe/Mn and Fe/Mg ratios of CSs. Based on measurements of isotopic compositions, Alexander et al. (2002) demonstrated that the evaporation of moderately refractory Mg remains fairly limited. In addition, Taylor et al. (2005) showed that Mn generally behaves as a refractory element, except when evaporation is persistent. In contrast, Fe may be lost through the ejection of Fe-Ni metal beads and/or evaporation and should thus be accounted for. Fig. 3a depicts the Fe/Mn and Fe/Mg ratios for the cosmic spherules characterized in this work. On this diagram, the loss of Fe shifts data points towards the origin. On the other hand, extensive evaporation will cause a particle to plot more towards the left since Mg is generally considered more refractory than Mn (Lodders, 2003). The majority of the spherules plot within or close to the chondritic field, in contrast to stony meteorite types which typically display lower Fe/Mn ratios relative to chondrites (Goodrich and Delaney, 2000; Lodders, 2003). Eight CSs studied here

are characterized by higher Fe/Mn or lower Fe/Mg ratios compared to those typically observed for chondrites. However, these values can result from (extensive) evaporation of chondritic material. On this plot, the white BO-type (WF1202B-0243), along with several V-types, plots close to the origin of the diagram, indicating that considerable Fe was lost through the ejection of (a) metal bead(s). The four BO-type CSs and the scoriaceous micrometeorite are positioned away from the origin, suggesting that they only experienced relatively small degrees of ejection/evaporation. However, a distinct trend from scoriaceous over PO-type, BO-type and CC-type to vitreous CSs cannot clearly be defined based on this diagram.

Cordier et al. (2011a) introduced a new classification for V-type CSs, based on their relative degree of evaporation. 'Normal chondritic' spherules are characterized by a variety of different colours based on their Fe content, with lower Fe-contents resulting in higher transparencies (Alexander et al., 2002). These particles have typically lost 40–50% of their mass due to evaporation during atmospheric entry heating based on chemical proxies (Cordier et al., 2011a). The 'CAT-like' spherules, not to be confused with CAT spherules, are oblate, colourless to pale green, with low Fe content (Fe/Si < 0.06), high MgO content (Mg/Si > 0.9) and relatively high Ti (Ti/Si ~ 0.004) and CaO + Al_2O_3 abundances (>5 wt%). Such particles have lost approximately 50–70% of their mass by evaporation based on the measured chemical ratios. 'High Ca-Al' spherules have been defined in Cordier et al. (2011a) as V-type spherules with CaO + Al_2O_3 concentrations >9 wt%, similar Ti contents as 'CAT-like' spherules, but higher Fe contents (Fe/Si > 0.06) and lower Mg abundances (Mg/Si < 0.9). These spherules have lost 80–90% of their original mass. Of the 44 vitreous CSs, two belong to the 'CAT-like' group, three correspond to the 'high Ca-Al' group and the remaining thirty-nine are identified as normal chondritic. Of the particles from the other textural groups, only the white BO-type (WF1202B-0243) micrometeorite is classified as 'CAT-like', while all other CSs in this study can be assigned to the 'normal chondritic' group.

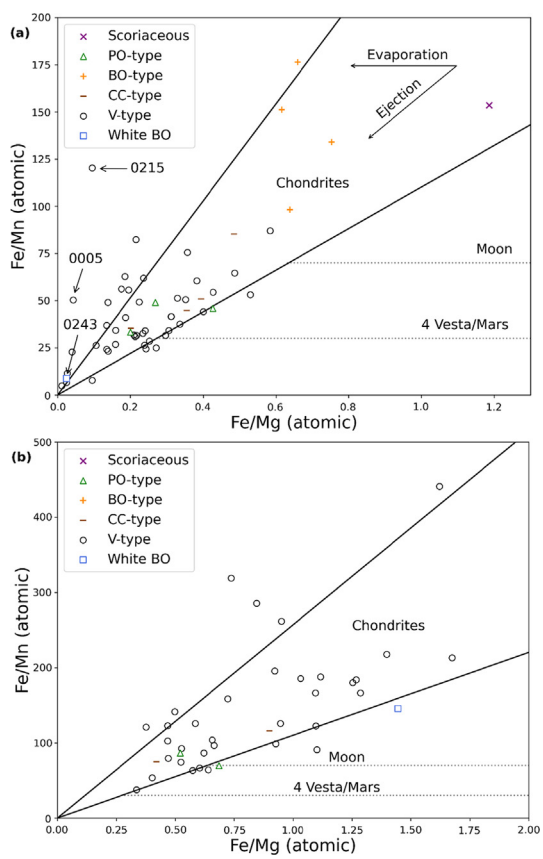

Fig. 3. (a) The Fe/Mg (atomic) vs. Fe/Mn (atomic) diagram provides an indication of the (non)chondritic nature of extraterrestrial material. Spherules with a high Fe/Mn relative to the chondritic field most likely experienced a high degree of chemical evaporation. Metal bead ejection moves spherules closer to the origin as it only reduces Fe and does not influence Mn or Mg significantly. (b) The Fe/Mg vs. Fe/Mn diagram with corrected Fe values, note that only spherules present in Table 2 have been plotted. Because of their high Fe/Mn ratios WF1202B-0005 (1275), WF1202B-0020 (620), WF1202B-0048 (620) and WF1202B-0215 (756) are not visible on the corrected diagram.

4.2. Nature of the Fe isotope fractionation process

The magnitude of isotope fractionation is positively correlated with the peak temperature and duration of heating experienced by the CS (Alexander et al., 2002). Mass-dependent fractionation can occur in two manners, either as kinetic fractionation or through equilibrium processes (e.g., Young et al., 2002; Goderis et al., 2016). Equilibrium fractionation is a quantum mechanical effect caused by the lower zero-point energies and vibrational frequencies of heavier isotopes in a molecule. Equilibrium fractionation takes place when there is chemical equilibrium between two different phases or compounds e.g., a fluid melt of a particle and the gaseous atmosphere, or a solid phase and the surrounding melt. It always strives towards a minimal total energy of the system (Young et al., 2002; Schauble, 2007). In contrast, kinetic fractionation occurs due to different reaction rates of isotopes or isotopologues with a different mass (Gussone et al., 2003). Heavier isotopes are generally mobilized by evaporation slower than lighter isotopes, and therefore, a residual particle has heavier isotopic compositions than an initial phase. The kinetic process is most commonly referred to as the cause of mass-dependent fractionation in CSs, as at characteristic timeframes and heating regimes equilibration is not expected. Moreover, at high temperatures magnitudes of equilibrium isotope fractionation are negligible (Young et al., 2002; Taylor et al., 2005; Pack et al., 2017). Rayleigh fractionation is often used to describe the evolution of an open system with two phases in which one phase is continuously removed from the system through fractional distillation, crystallization or condensation. In particular, Rayleigh fractionation has been used to describe a specific case of kinetic isotope fractionation where material is evaporated at high temperature and the vapour phase is removed irreversibly. Both equilibrium and kinetic fractionation processes result in a change of isotope ratios based on the

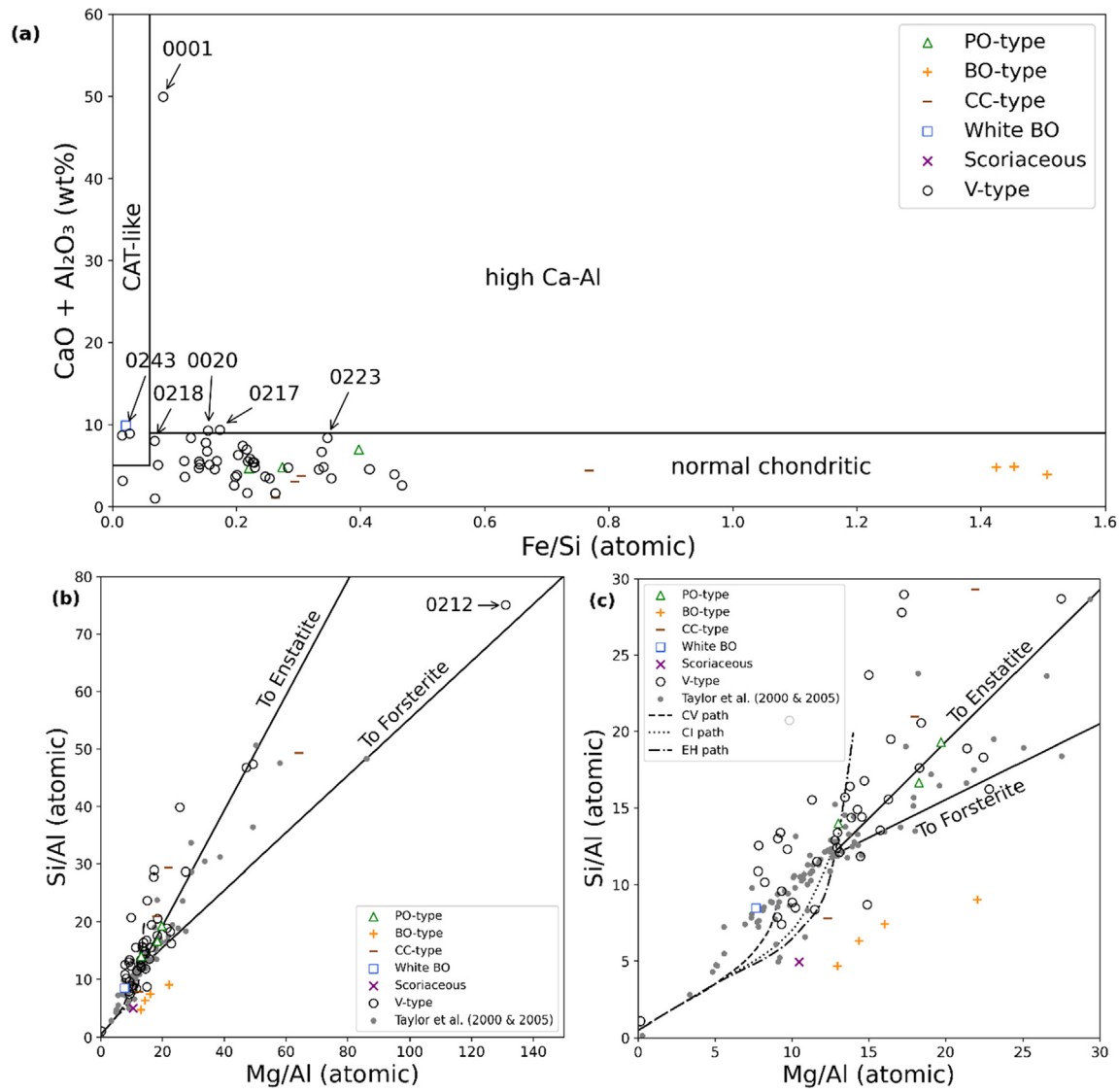

Fig. 4. (a) The chemical classification as proposed by Cordier et al. (2011a, 2011b). (b & c) The Si/Al (atomic) versus Mg/Al (atomic) diagram for data from this work and Taylor et al. (2000 & 2005), the pathways are reconstructed from Alexander et al. (2002).

masses of the isotopes, but the functional forms of the fractionation laws are slightly but distinctly different (Young et al., 2002). The extreme magnitude of isotope fractionation of Fe in the CS, together with high precisions of the isotope ratios, allows to investigate the nature of the fractionation processes taking place. According to Young et al. (2002), the fractionation exponent β, characterizing the nature of the actual mass-dependent fractionation process (equilibrium or kinetic fractionation), can be calculated as the slope of the linearized three isotope plot in logarithmic scale using δ^{i}Fe notations (Eq. (1)).

$$\delta^{i}Fe = 1000 * \ln\left(\frac{{}^{i}Fe/{}^{54}Fe_{sample}}{{}^{i}Fe/{}^{54}Fe_{reference\ \ material}}\right) \quad (1)$$

Where ^{i}Fe represents the abundances of the ^{56}Fe or ^{57}Fe isotopes. IsoplotR 3.7 offers several options to regress the measured isotopic ratios in the 3-isotope plot, taking into account the analytical uncertainties for example using the York algorithm, model-2, or robust regression. The regression algorithm of York assumes that analytical uncertainties are naturally distributed and calculates the weighing factors for each point in the 3-isotope plot reversely proportional to its ascribed uncertainty. The algorithm assumes that analytical uncertainty is the only contributor to scatter between the data points. If this assumption is correct, the mean squared weighted deviation (MSWD) will be below 1 (York et al., 2004; Vermeesch, 2018). Due to several data pairs having unrealistically low random uncertainties, the maximum likelihood algorithm of line fitting results in a slightly elevated MSWD of 1.7, suggesting that York's algorithm is not an appropriate choice for line fitting in this case. As such, the model-2 and the robust regression fitting algorithms of IsoplotR 3.7 were used instead (Fig. 6). The robust

regression algorithm avoids any assumption of an uncertainty and calculates the slope as the median of all pairwise slopes (Theil, 1992), with errors calculated according to Rock and Duffy (1986) after Vugrinovich (1981). This model is suited in situations of elevated scatter, with MSWD $\gg$ 1. Alternatively, the model-2 algorithm is most suited for cases where it is clear that the analytical uncertainties are not the main source of scatter. To avoid weighting the points according to analytical errors, the model-2 algorithm assigns equal weights and zero error-correlations to each point, and instead of the analytical uncertainties the 95% confidence-limit uncertainties are calculated from errors including scatter multiplied by student's coverage factor (Ludwig, 2008). The model-2 and the robust regression algorithms provide nearly equal regression slopes (1.4850 ± 0.0053 and 1.4913 + 0.011/−0.0052, 95% CI) and MSWD < 1. The theoretical fractionation exponents of the kinetic and equilibrium isotope fractionation processes are given in Eqs. (2a) and (2b) (Wombacher and Rehkämper, 2003; Audi et al., 2003). As the experimental fractionation exponent is equivalent to the kinetic constant within the confidence interval, kinetic processes, such as evaporation or diffusion, are the main contributors to the extreme isotope fractionation of Fe found in a fraction of the CSs studied here, rather than equilibrium processes, such as metal bead extraction. Despite the large variation in Fe isotope fractionation, the precision of the determined fractionation exponent β does not allow to differentiate between evaporation of atomic Fe or Fe isotopologues, such as FeO (Eq. (2c)), which is in agreement with the recent findings of Fischer et al. (2021).

$$\beta_{kin} = \frac{\ln\left(\frac{m^{Fe_{54}}}{m^{Fe_{57}}}\right)}{\ln\left(\frac{m^{Fe_{54}}}{m^{Fe_{56}}}\right)} = 1.4881 \tag{2a}$$

$$\beta_{eq} = \frac{\ln(1/m^{Fe_{54}} - 1/m^{Fe_{57}})}{\ln(1/m^{Fe_{54}} - 1/m^{Fe_{56}})} = 1.4750 \tag{2b}$$

$$\beta_{kin,FeO} = \frac{\ln(m^{Fe_{54}} + m^{O_{16}}/m^{Fe_{57}} + m^{O_{16}})}{\ln(m^{Fe_{54}} + m^{O_{16}}/m^{Fe_{56}} + m^{O_{16}})} = 1.4910 \tag{2c}$$

In nature, kinetic isotope fractionation is known to occur during the processes of evaporation/condensation and diffusion. Although evaporation due to extreme heating during atmospheric entry is the most obvious cause for the isotope fractionation observed, here we evaluate the possibility that a part of the isotope fractionation results from diffusion. While there is no concentration gradient in a (relatively) homogeneous sphere during atmospheric passage to drive chemical diffusion, diffusion can also occur as the result of thermal gradients. The Soret effect is a process in which different ions and isotopes are transported in liquid at different speeds under the force of a thermal gradient (Richter et al., 2009a). During atmospheric entry, the outer part of the melted CS experiences frictional heating due to gas drag and is hotter compared

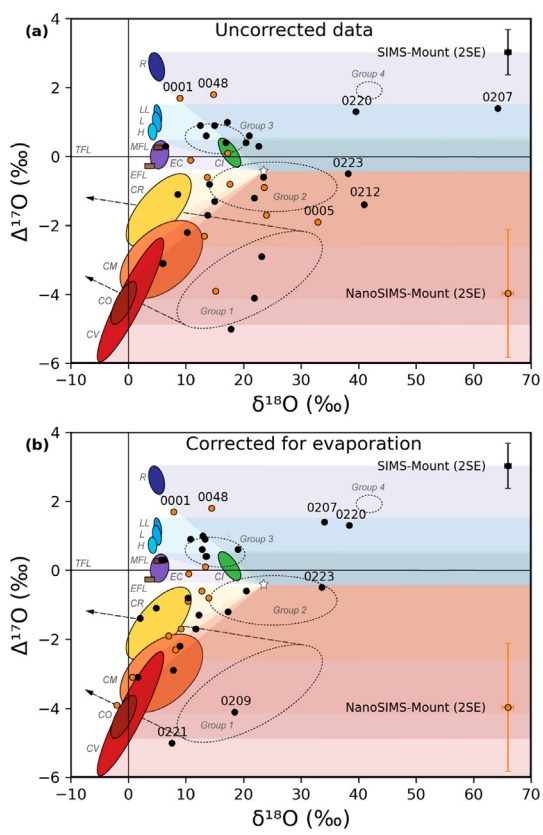

Fig. 5. Plot of measured $\Delta^{17}O$ versus $\delta^{18}O$ (a) and the same plot after correction for evaporation based on $\delta^{57}Fe$ (b). These diagrams can be used to (i) determine the relative degree of isotope fractionation and mixing, and (ii) derive the precursor bodies from which the particles derived, modified from Suavet et al. (2010) and Goderis et al. (2020), the 'Group' fields are based on those identified by Suavet et al. (2010). The precursor body fields are defined in Suavet et al. (2010) that drew lines around classes of WR measurements on different meteorite types from Clayton et al. (1991), Clayton and Mayeda (1999) and Newton et al. (2010).

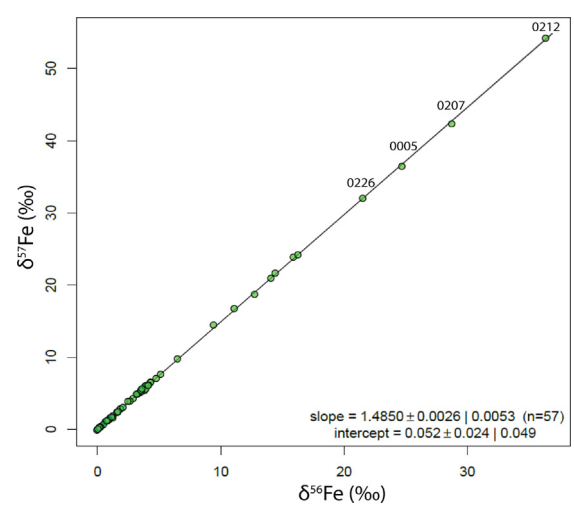

Fig. 6. The $\delta^{56}Fe$ vs $\delta^{57}Fe$ diagram of the CSs mentioned in this work; the slope has been calculated using the 'model-2' method of IsoplotR 3.7. The slope corresponds within uncertainty with the theoretical value for kinetic isotope fractionation i.e., 1.4881.

to the inner volume. As observed in experimental work, Ti, Mg, Fe and Al will concentrate towards the colder centre, while Si, Na and K migrate towards the hotter surface of an initially homogeneous melted spherule (Lesher and Walker, 1986). Despite the limited number of experiments in literature, relatively large isotope fractionation effects have been observed as the result of thermal diffusion. The Fe isotopic composition of the hotter end of a basalt sample that was run in a piston cylinder with a temperature gradient of 1410–1520 °C was found to be significantly isotopically lighter than that of the colder end (Richter et al., 2008; Richter et al., 2009a; Richter et al., 2009b). The thermal fractionation of the Fe isotopes was calculated to be 1.1‰ per atomic mass unit per 100 °C of the gradient, and the magnitude of the isotope fractionation is, to a first order, distributed as a linear function of ΔT, nearly independently of the composition of the melt (Huang et al., 2010; Richter, 2011). The thermal gradient of a few hundred K between the inner and outer parts of the spherule can thus correspond to Fe isotope fractionation by several per mille, which is still considerably smaller than the magnitudes of the effects observed in this work. However, if the diffusion in a sub-mm melted particle can be considered instantaneous, continuous removal of the hotter outer side, where Fe is a few per mille lighter, can hypothetically result in a progressive Rayleigh-like isotope fractionation process

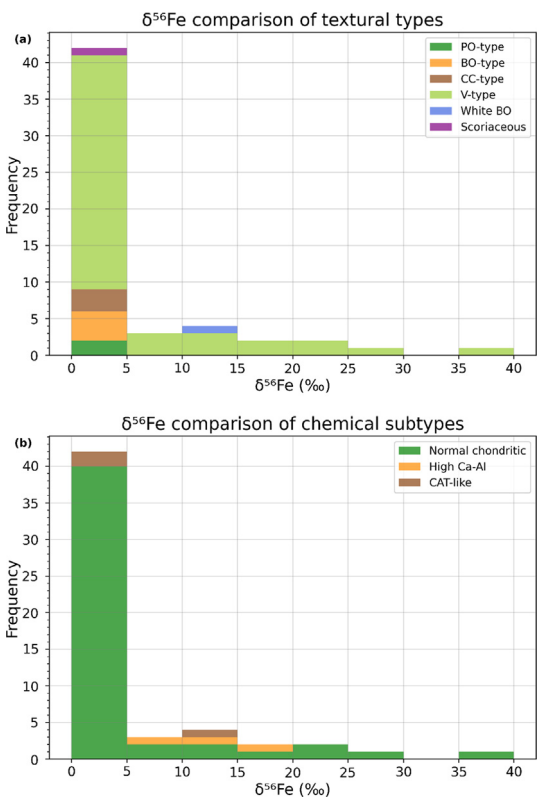

Fig. 7. Frequency (count) histograms of the δ^{56}Fe distribution in the (a) textural subtypes and (b) chemical subtypes.

that can lead to a significantly heavier Fe isotopic composition of the remaining melt. This process takes place in the same direction as the isotope fractionation by evaporation. At the same time, such process would lead to a depletion of the CSs in Na, K, and Si, which is in agreement with the observations. However, the contribution of Soret diffusion to the depletion of volatile elements and the isotope fractionation of Fe relative to thermal evaporation remains unclear, as the thermal parameters of the micrometeorites during atmospheric entry are difficult to constrain and require the determination of the isotope ratios of multiple elements at high precision in individual particles, which may require considerable instrumental advances still.

However, it is possible to compare the distinct textural and chemical subgroups based on their δ^{56}Fe values (Table 1, Fig. 7). The average δ^{56}Fe ± 2SD for the scoriaceous (0.0 ± 0.1‰), PO (0.3 ± 0.9‰), BO-type (0.8 ± 0.6 ‰), CC-type (1.0 ± 3.4‰) and V-type (6.6 ± 16.5‰) textural subgroups indicate an overall increasing trend of the mean values from scoriaceous to V-type particles. However, the associated 2SD uncertainties, reflecting the variability within each group, overlap between many of the subgroups, which prevents conclusive statements. The V-type spherules are characterised by the largest spread (δ^{56}Fe of 0.17 ± 0.22‰ to 37.01 ± 0.35‰) in Fe signatures, while the mean ± 2SD and median of this subgroup lie at 6.7 ± 17.0‰ and 3.42‰, respectively. The 'normal chondritic' V-type subgroup is characterised by an average δ^{56}Fe ± 2SD of 6.6 ± 17.6‰ (with a range of 0.17–37.01‰, n = 32), the 'CAT-like' 10.9 ± 11.3‰ (5.1–16.4‰, n = 3) and the 'high Ca-Al' 5.5 ± 14.9‰ (1.2–14.2‰, n = 3). Based on the measured data set, the expected trend in increasing isotope fractionation from 'normal chondritic' spherules, over 'CAT-like' spherules to the 'high-Ca-Al' subgroup is not observed for the average values of our results. The mechanism of ablation prior to evaporation can strongly influence these isotopic signatures and cannot be fully quantified (Section 4.3; Fig. 1). If thermal evaporation is the dominant process affecting the Fe isotope signatures of CSs, then these results may indicate that the textural subgroups have experienced varying degrees of thermal evaporation, while this does not appear to be the case for the chemical subgroups. This suggests that it is not possible to correlate the degrees of chemical and isotope fractionation in individual particles as these processes appear to be unrelated to one another (Fig. 8a). Here, it is worth noting that no correlation between isotope fractionation (δ^{56}Fe) and volatile element contents (K, Na and Zn) can be observed either (Fig. 8b–d; Supplementary Fig. EA2). As chemical fractionation might be influenced significantly by precursor composition, mineralogical biases, fragmentation, high-density phase expulsion, and secondary alteration, isotope fractionation may reflect a more representative proxy to estimate the total extent of evaporation experienced by the particle than chemical fractionation. At the same time, isotope fractionation depends on a series of factors as well, including the initial mineralogy of the micrometeorite, melt composition, redox conditions, etc. but perhaps to a lesser degree, as evidenced by the extreme magnitudes of isotopic

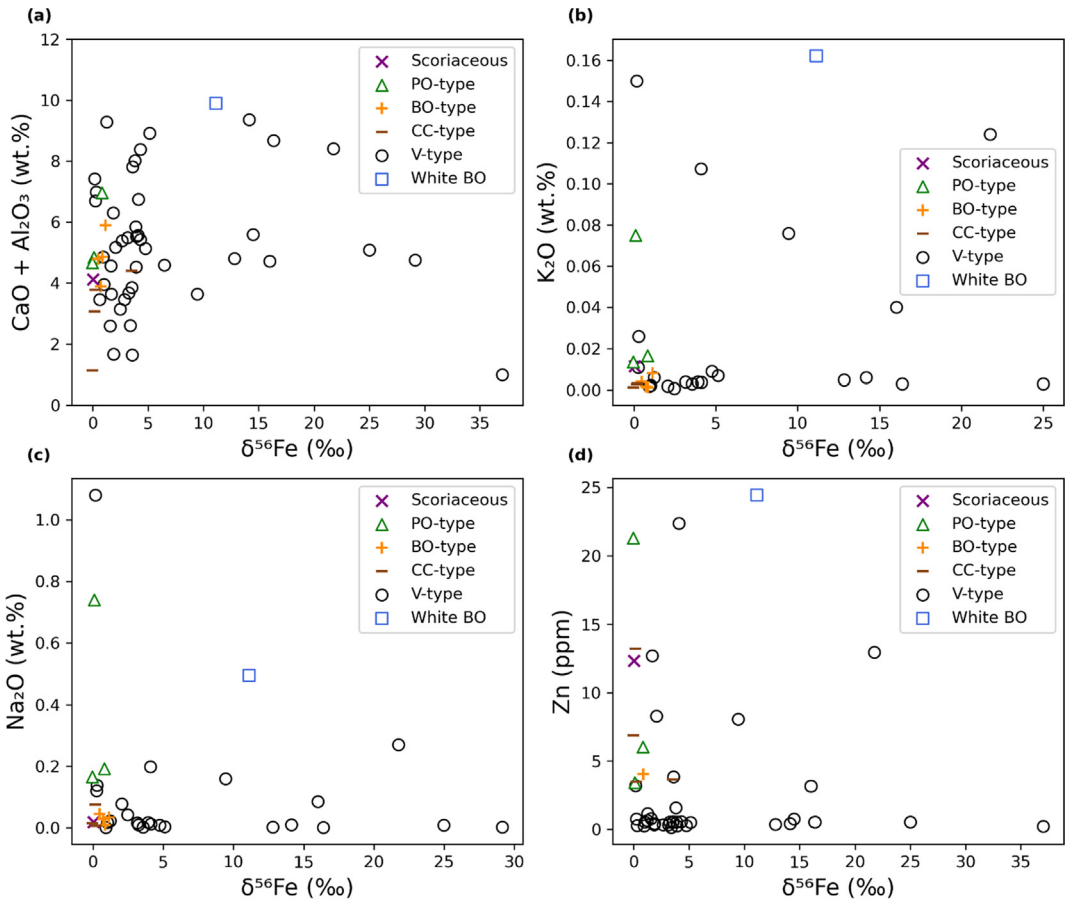

Fig. 8. (a) Plot of δ^{56}Fe (in ‰) versus CaO + Al_2O_3 (in wt.%), with no distinct correlation indicating that these do not both reflect evaporation. Note that spherule WF1202B-0001 is not visible in this diagram, as it has a CaO + Al_2O_3 of ~50 wt% (and δ^{56}Fe of ~1‰). (b–d) Similar diagrams comparing K_2O, Na_2O and Zn concentrations to δ^{56}Fe. None of these show a significant correlation.

signatures. The correlation between the fractionation of Fe and O isotopes is discussed in detail in Section 4.4.

4.3. Fe loss by evaporation and metal bead ejection

If the loss of Fe in CSs is dominated by evaporation and metal bead ejection, the respective fractions lost by these processes experienced by a CS upon atmospheric entry can theoretically be approximated (Alexander et al., 2002; Taylor et al., 2005), allowing to reconstruct the original chemical compositions of the particles, which may provide valuable information on the precursor materials. This quantification of Fe loss for a larger set of samples improves our understanding of the relative importance of these distinct processes taking place during atmospheric entry.

Fig. 1 depicts two extreme pathways through which a particle with an initial Fe-content and δ^{56}Fe can arrive at a final (i.e., the observed) Fe content and δ^{56}Fe. Following metal bead ejection, only the Fe content of a micrometeoroid decreases, while the δ^{56}Fe values of a particle are not altered significantly during this process. On the other hand, evaporation lowers the Fe content and increases the δ^{56}Fe values of an incoming micrometeoroid. Because of these effects, the amounts of evaporation and ejection can be calculated according to distinct pathways. Based on the set of equations published in Alexander et al. (2002) and Taylor et al. (2005), it is possible to calculate the amount of Fe that was lost, as well as the hypothetical minimum and maximum amounts of evaporation and ejection that a particle experienced during atmospheric passage. In the case of a fraction of the particles studied here, the results for such calculations remain inconclusive, which can potentially be attributed to the assumption of a CM-like heritage for all spherules in these models. The assumption of a CM-like heritage is needed because the initial Fe/Al ratios are an additional unknown in the model calculation, and the Fe/Al ratio of CM-like material is as such assumed to be a valid approximation for most extraterrestrial materials. However, when the precursor composition of the studied particles deviates significantly from that of CM-like material, this assumption is evidently incorrect and the resulting model invalid (Alexander et al., 2002; Taylor et al., 2005). The calculations that have proven to be meaningful are summarized in Table 2 and have been used to calculate the initial Fe/Mg vs. Fe/Mn atomic

ratios of the CSs (Fig. 4b). Based on these results, CSs appear to have lost between virtually 0 and 59% of their initial Fe through evaporation, while between 4 and 99% of their initial iron mass escaped through the ejection of Fe-Ni beads. The fractions of Fe lost by evaporation/ejection calculated using the two extreme pathways are generally in good agreement when evaporation is limited and the Fe isotope fractionation is small (δ^{56}Fe < ~3‰). When fractionation is high, the modelled pathways deviate more substantially. An independent evaluation of these models is provided by the analysis of O isotope measurements in Section 4.4.

4.4. Constraints on CS precursor materials

Oxygen isotope ratios are often used to identify precursor bodies of micrometeorites (Taylor et al., 2005; Suavet et al., 2010; Cordier et al., 2011a; Goderis et al., 2020; Rudraswami et al., 2020; Soens et al., 2020). In order to determine the corresponding parent body of each micrometeorite, a plot of δ^{17}O versus δ^{18}O, or the more common Δ^{17}O vs. δ^{18}O diagram is used, where $\Delta^{17}O = \delta^{17}O - 0.52 * \delta^{18}O$ represents the deviation from the Terrestrial Fractionation Line (TFL; Fig. 5a; Thiemens et al., 1983; Rumble et al., 2007). This method is based on the principle that each type of parent body is characterized by a distinct oxygen isotopic signature, inherited from the nebular stage (Clayton et al., 1976; Suavet et al., 2010). Three processes can modify the original oxygen isotopic signature of a micrometeorite, characteristic for the parent body. Firstly, mass-dependent fractionation during atmospheric entry enriches the particle in the heavier oxygen isotopes, effectively shifting data points to the right on a plot of Δ^{17}O versus δ^{18}O (Suavet et al., 2010). Secondly, mixing with atmospheric oxygen during atmospheric entry shifts the oxygen isotope ratios along the mixing line towards isotopic signatures of the atmosphere ($\delta^{17}O \approx 11.8$‰ and $\delta^{18}O \approx 23.5$‰), which is isotopically homogeneous and thought not to have changed significantly over the past couple of Myr (Thiemens et al., 1995; Pack et al., 2017; Fischer et al., 2021). Lastly, terrestrial alteration can also influence the original oxygen isotope ratios. Since all spherules selected for oxygen isotope analysis were extracted from the same sedimentary accumulation trap in the Sør Rondane Mountains (Antarctica), alteration would shift the CS composition to the right of the surrounding meteoric water along the TFL, with an average δ^{18}O of roughly −30‰, following the formation of secondary minerals (Goderis et al., 2020). Taking these processes into account, four groups of CSs with distinct oxygen isotopic values have previously been identified (Fig. 5a; Suavet et al., 2010).

Comparison between the iron (δ^{56}Fe, δ^{57}Fe) and oxygen (δ^{17}O, δ^{18}O) isotope ratios indicates that for most spherules a positive correlation exists between the two isotope systems (Fig. 9). This correlation is mainly influenced by two processes, i.e., mass-dependent fractionation and mixing with atmospheric oxygen. Mass-dependent fractionation will increase both δ^{18}O and δ^{56}Fe values, while mixing with atmospheric oxygen only increases the δ^{18}O values. It is important to remark that precursor δ^{18}O values for the different types of chondritic bodies span a broad range from −5‰ up to +10‰ (Fig. 9). However, the majority of chondritic fields has an initial δ^{18}O between 0 and 5‰, which narrows this range down significantly. On Fig. 9, two trends are observed: (i) the first consists of a wide spread of CSs that predominantly experienced mass-dependent fractionation during evaporation, while (ii) the second trend is represented by spherules that are characterized by low δ^{56}Fe values and δ^{18}O of ~12–23‰, indicating that mixing with atmospheric oxygen is the main process modifying the δ^{18}O of these spherules. Of the thirty-six spherules that have both O and Fe isotope ratios measured, only nine exhibit δ^{56}Fe values above 9‰. One of those is WF1202B-0207, which presumably has a different initial δ^{18}O value ('Group 4') and is therefore excluded from the observed trend. The remaining eight CSs all define a correlation with δ^{18}O that can be used to calculate a correction factor ($R^2 = 0.809$) for mass-dependent isotope fractionation as the result of evaporation during atmospheric passage, following Eq. (3).

$$\delta^{18}O_{corr} = \delta^{18}O_{meas} - 1.044 * \delta^{56}Fe_{meas} \quad (3)$$

This correction does not consider any effects from mixing with atmospheric oxygen or subsequent terrestrial alteration. Indeed, the CSs are relatively unaltered (Supplementary Table EA1) and the latter process can largely be disregarded. As evaporation is a mass-dependent process, no deviation from the TFL will occur during evaporation and any deviation from the original Δ^{17}O will result from mixing with atmospheric O. The $\delta^{18}O_{corr}$ is plotted versus Δ^{17}O in Fig. 5b in order to improve identification of the parent bodies of the CS. The isotopic ratios of spherule WF1202B-0223 (δ^{18}O of ~38‰, Δ^{17}O of ~−0.5‰ and δ^{57}Fe of ~5‰) cannot be explained by the combination of fractionation and mixing. Most likely this particle could be derived from a rare precursor body (e.g., CY) or an unknown third process has influenced the isotopic composition of this particle. Of the 36 spherules measured for oxygen isotopes, twenty could not be classified within the 95% certainty interval, fourteen can be regarded as CC and two as Group 4 (Table 1; Fig. 5b). However, by combining the Δ^{17}O with the Fe-corrected δ^{18}O, a subset of the twenty 'ambiguous' CSs can also tentatively be classified. As such, particles WF1202B-0005, WF1202B-0020 and WF1202B-0202 may be of CC parentage, six spherules (with $\delta^{18}O_{corr}$ of 10.8–13.6‰ and Δ^{17}O of 0.4–1.0‰) from the SIMS-mount plot very close to the OC fields and two samples from the SIMS-mount (WF1202B-0205 and WF1202B-0211) appear to fall within the EC field. Furthermore, the improved classification allows to assign one of the CC CSs (WF1202B-0212) more specifically to the CR chondrite group. The sizes of the CSs that appear to be related to CC range from 215 to 764 μm, while the ones possibly related to OCs fall within a narrow range of 208–287 μm (Supplementary Table EA2).

The 'Group 4' cosmic spherules are hypothesised to represent a chondritic parent body currently not sampled by larger meteorites (Suavet et al., 2010; van Ginneken et al.,

Table 2
Evaporation and ablation as calculated with the formulas of Alexander et al. (2002) and Taylor et al. (2005).

Sample name	δ^{57}Fe (‰)	f_{ret} [a]	f_{ret} [b]	Evaporation precedes ablation		Ablation precedes evaporation	
				Fe [c]	Fa [c]	Fe [d]	Fa [d]
WF1202B-0226	0.10	0.99	1.00	0.00	0.38	0.00	0.38
WF1202B-0233	0.22	0.99	0.99	0.01	0.25	0.01	0.25
WF1202B-0021	0.25	0.99	0.99	0.01	0.66	0.00	0.67
WF1202B-0004	0.29	0.98	0.98	0.01	0.77	0.00	0.78
WF1202B-0205	0.43	0.99	0.99	0.01	0.69	0.00	0.69
WF1202B-0210	0.69	0.96	0.98	0.02	0.28	0.02	0.29
WF1202B-0228	0.82	0.96	0.97	0.03	0.32	0.02	0.33
WF1202B-0039	0.93	0.95	0.95	0.03	0.61	0.01	0.63
WF1202B-0220	1.06	0.94	0.96	0.04	0.13	0.03	0.14
WF1202B-0217	1.21	0.93	0.96	0.04	0.81	0.01	0.85
WF1202B-0001	1.23	0.94	0.94	0.04	0.95	0.00	0.99
WF1202B-0224	1.56	0.91	0.94	0.06	0.04	0.05	0.04
WF1202B-0213	1.60	0.91	0.94	0.06	0.36	0.04	0.38
WF1202B-0238	1.66	0.91	0.94	0.06	0.56	0.02	0.60
WF1202B-0204	1.77	0.90	0.94	0.06	0.48	0.03	0.51
WF1202B-0237	2.06	0.89	0.93	0.07	0.59	0.03	0.63
WF1202B-0239	2.46	0.86	0.91	0.09	0.86	0.00	0.94
WF1202B-0219	2.66	0.86	0.91	0.09	0.51	0.04	0.56
WF1202B-0202	2.76	0.85	0.90	0.10	0.12	0.09	0.14
WF1202B-0024	3.16	0.83	0.84	0.11	0.73	0.02	0.82
WF1202B-0209	3.26	0.83	0.89	0.11	0.42	0.06	0.48
WF1202B-0222	3.42	0.82	0.88	0.12	0.40	0.07	0.45
WF1202B-0236	3.52	0.82	0.88	0.12	0.18	0.10	0.21
WF1202B-0241	3.61	0.81	0.88	0.12	0.70	0.02	0.80
WF1202B-0218	3.73	0.82	0.87	0.13	0.78	0.01	0.90
WF1202B-0012	3.92	0.81	0.82	0.13	0.56	0.05	0.65
WF1202B-0208	4.02	0.80	0.87	0.13	0.55	0.05	0.63
WF1202B-0242	4.10	0.80	0.86	0.14	0.60	0.04	0.70
WF1202B-0240	4.13	0.79	0.86	0.14	0.58	0.04	0.68
WF1202B-0216	4.26	0.80	0.87	0.13	0.54	0.05	0.62
WF1202B-0206	4.31	0.78	0.86	0.14	0.48	0.06	0.56
WF1202B-0223	4.35	0.78	0.85	0.15	0.47	0.07	0.55
WF1202B-0009	4.76	0.77	0.77	0.16	0.67	0.03	0.80
WF1202B-0010	5.13	0.75	0.76	0.17	0.81	0.00	0.98
WF1202B-0214	6.80	0.69	0.79	0.21	0.45	0.09	0.57
WF1202B-0221	9.43	0.58	0.71	0.29	0.32	0.16	0.45
WF1202B-0243	11.14	0.53	0.67	0.33	0.65	0.01	0.97
WF1202B-0019	12.82	0.50	0.51	0.37	0.29	0.20	0.47
WF1202B-0215	13.90	0.44	0.59	0.41	0.43	0.11	0.73
WF1202B-0020	14.16	0.46	0.47	0.40	0.50	0.07	0.83
WF1202B-0211	16.25	0.41	0.56	0.44	0.29	0.21	0.51
WF1202B-0048	16.38	0.40	0.41	0.45	0.54	0.01	0.98
188-5	21.74	0.30	0.46	0.54	0.33	0.15	0.73
WF1202B-0005	24.99	0.26	0.26	0.59	0.36	0.07	0.88

[a] Fraction of the initial Fe retained in the particle, the Rayleigh evaporation law: $f = (\varphi/1000 * (Y\text{-}A) + 1)^{(1/(1/\alpha-1))}$ was implemented to calculate these results. φ equals δ^{57}Fe/(Y-A) with Y the atomic mass of ^{57}Fe and A the atomic mass of ^{54}Fe. α is ^{57}Fe/^{54}Fe isotope fractionation factor which equals 1.0274 (Wang et al., 1994).

[b] Fraction of the initial Fe retained in the particle, calculated from the measured Fe/Al (mass ratio), assuming the initial Fe/Al ratio of CM-chondrite.

[c] Fraction of the lost Fe which evaporated (Fe) or was lost via ablation/ejection (Fa) when evaporation precedes ablation entirely.

[d] Fraction of the lost Fe which evaporated or was lost via ablation/ejection when ablation precedes evaporation.

2017; Suttle et al., 2020). In our dataset at least one particle (WF1202B-0220) belongs to the 'Group 4' micrometeorites. To further strengthen the hypothesis that this 'Group 4' effectively represents a separate cluster (Fig. 5), the Fe isotopic data of spherules WF1202B-0220 and WF1202B-0207 are discussed here. Spherule WF1202B-0220 has δ^{56}Fe and δ^{57}Fe values of 1.02‰ and 1.61‰, respectively, implying that the chemical and isotopic composition has not been affected significantly by evaporation. Spherule WF1202B-0207 on the other hand shows extremely fractionated Fe isotope ratios (δ^{56}Fe = 29.14‰ and δ^{57}Fe = 43.23‰), with a δ^{18}O of 64.24‰ relative to the average 40–45‰ for 'Group 4'. The corrected δ^{18}O plot (Fig. 5b) suggests that this particle is in fact also a 'Group 4' spherule

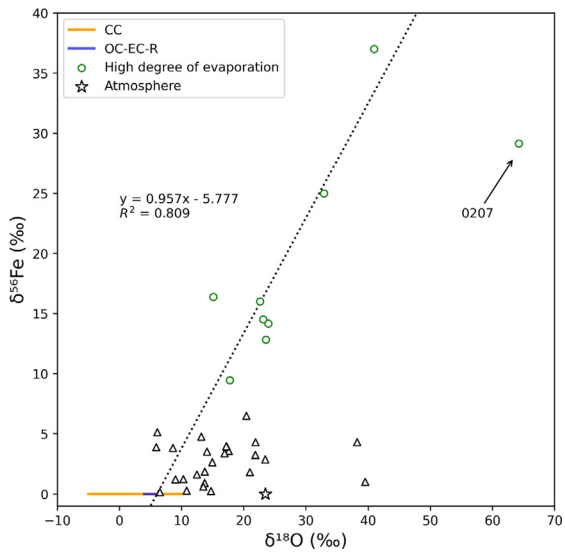

Fig. 9. Plot of δ^{56}Fe (in ‰) versus δ^{18}O (in ‰). The spherules in green, with the exception of WF1202B-0207, were used to construct the evaporation slope. 'CC' indicates the initial δ^{18}O and δ^{56}Fe range of carbonaceous chondrites, while 'OC-EC-R' shows the same initial ranges for ordinary chondrites, enstatite chondrites and Rumuruti chondrites.

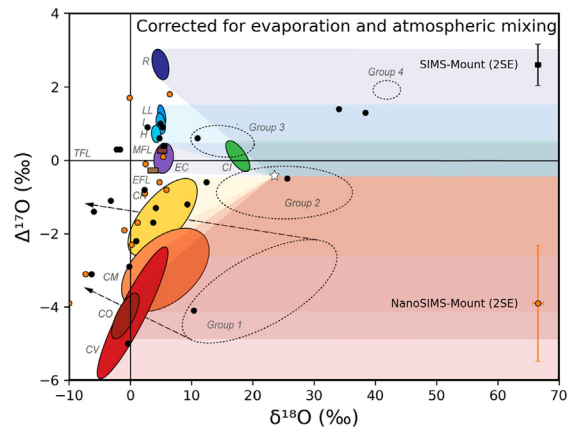

Fig. 10. Diagram of Δ^{17}O versus δ^{18}O corrected for evaporation (based on δ^{56}Fe) and atmospheric mixing. The ~8‰ correction for atmospheric mixing was not applied on the Group 4 CSs, as the correction is expected to be in the opposite direction with an unknown magnitude.

that has undergone extensive evaporation and some mixing with atmospheric oxygen. The presence of both an unfractionated and fractionated particle of this nature confirms that this denotes a separate group and that it is not for example a cluster of fractionated OCs. Fig. 3 and Supplementary Fig. EA1 indicate that these particles are chondritic in nature, which is in agreement with the observations made by Suttle et al. (2020).

By studying the fusion crusts of I-type CSs, Clayton et al. (1986) observed that atmospheric mixing induces a ~8‰ shift in δ^{18}O for I-type CSs. Subsequently, this value was applied to correct the effect of atmospheric mixing on δ^{18}O of achondritic CSs (Cordier et al., 2012). Here, we evaluate the use of this correction for chondritic S-type CSs. From Fig. 5b, it can be observed that the CSs that are hypothesised to be linked to OCs (outside of the 95% confidence interval) have δ^{18}O values of 10.8–13.6‰, which is ~8‰ more positive than the fields of the OC precursor bodies (3–8‰). The CSs from other precursor bodies (CC, EC, and Group 4 particles) do not appear to cluster ~8‰ to the right of their original field, and while more particles plot within or closer to the CC and EC fields following the atmospheric correction, several particles also plot to the left of the CC fields when applying an ~8‰ shift (Fig. 10). It is worth mentioning that the two potential EC CSs (outside of the 95% confidence interval) have similar Δ^{17}O and δ^{18}O values as their precursor bodies before applying an atmospheric correction. Spherules WF1202B-0012, WF1202B-0201 and WF1202B-0214, which are classified as ambiguous with small positive Δ^{17}O values, have a similar δ^{18}O as the OC CSs, and plot within the EC field when corrected for atmospheric mixing. The large uncertainties on the Δ^{17}O preclude them from being assigned to either the OC or EC parent bodies. The low number of (potential) EC CSs in our dataset along with the lack of literature data prevents any conclusive statements, and further research will need to determine whether EC CSs experience similar degrees of evaporation and atmospheric mixing or not. Based on our work, at least a fraction of the chondritic materials that enters the Earth's atmosphere (i) did not experience a positive shift in δ^{18}O of ~8‰ due to mixing with atmospheric oxygen, which may be linked to the oxidation state of the precursor body or a differential response of the precursor mineralogy to atmospheric heating, (ii) displayed a starting composition to the left of the established meteorite parent bodies, or (iii) experienced a shift to the left due to variable alteration during the terrestrial residence of the CSs (cf. Goderis et al. 2020).

The correction for atmospheric mixing allows to evaluate the theoretical fraction of O which was evaporated (Cordier et al., 2012). This calculated fraction based on O can be compared to that based on Fe (Fig. 11). While the fraction of O that evaporated is systematically larger than that of Fe, which is to be expected as O is more volatile than Fe, these fractions largely co-vary. This co-variation thus largely confirms the validity of the applied equations for calculating the fractions of O and Fe that evaporated, and emphasises the importance of the precursor composition on the degree of evaporation experienced.

5. CONCLUSIONS

The main goal of this work was to gain further insights into the processes affecting micrometeoroids during atmospheric passage. This was achieved through the analysis of the major element composition, combined with iron and oxygen isotopic data. Based on the Fe isotopic data, kinetic fractionation has been identified as the dominant process causing extreme mass-dependent isotope fractionation in micrometeoroids during atmospheric entry. The origin of this fractionation is likely thermal evaporation, although the Soret effect and continuous ablation of the overheated exterior of the melted spherule might represent

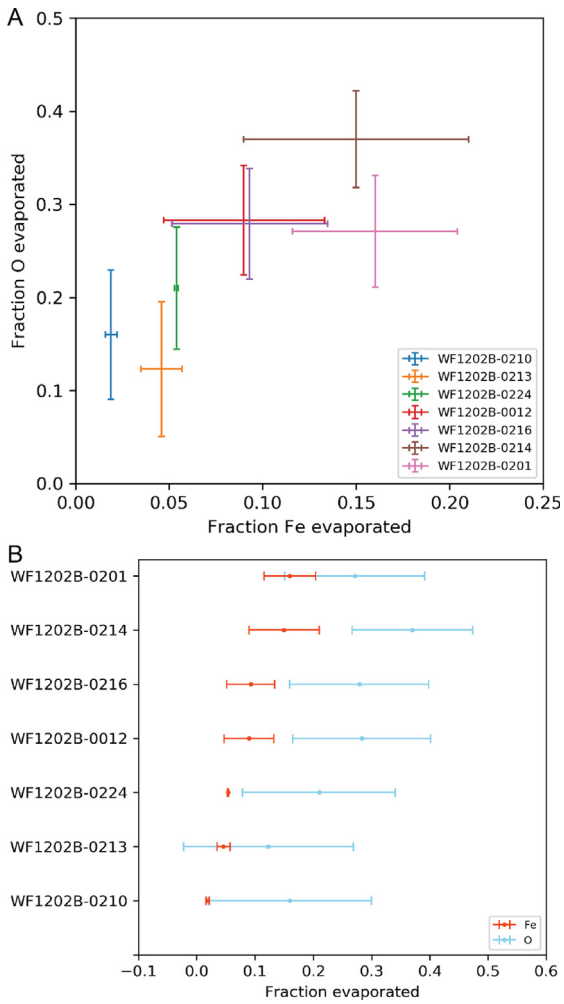

Fig. 11. (a) The evaporated fraction calculated based on O isotopes versus that based on Fe isotopes. (b) spherule-based comparison of the fractions of Fe and O that evaporated. Only the four OCs and three ambiguous spherules that have a high probability of deriving from OC parent bodies have been considered here as the 'atmospheric correction method' only appears to be applicable to OCs.

an alternative or contributing isotope fractionation mechanism. Mass-dependent isotope fractionation shows an overall increasing trend in the mean δ^{56}Fe values from scoriaceous to PO-type over BO-type and CC-type towards V-type, although the ranges of the textural groups overlap. Similar to the V-type CSs that display δ^{56}Fe between <1‰ and >30‰, the single white BO-type particle analysed here following acid digestion and Fe isolation also displays a relatively high δ^{56}Fe value of ~11‰. Furthermore, comparison of chemical fractionation based on Zn, Na_2O, K_2O, CaO or Al_2O_3 concentrations with isotope fractionation indicates that no substantial correlation between these two processes exists, implying that either both isotope fractionation and chemical evaporation are largely controlled by distinct processes, or that chemical fractionation cannot be estimated correctly due to random mineralogical effects on the initial compositions of these CSs (as a result of their small size). Based on the particles studied here, evaporation contributes up to ~60% of the Fe loss, while Fe-Ni-bead ejection during atmospheric entry can vary from no noticeable effect to the entire loss of all Fe from a CS (i.e., 0 to virtually 100%).

A second goal of this work was to refine the linkage of CSs to their appropriate precursor bodies. Based on Fe/Mn vs. Fe/Mg ratios and other compositional characteristics, all micrometeorites studied in this work are chondritic in nature. By studying the oxygen isotope ratios of vitreous CSs on a modified three oxygen isotope plot (Δ^{17}O vs. δ^{18}O), fourteen particles could be linked to a CC heritage within the 95% confidence interval, while an additional three CSs fall just below the 95% interval. Furthermore, one of the CCs could be more precisely identified as part of the CR subtype. However, the classification of several spherules remains ambiguous, in part due to significant analytical uncertainties. Importantly, the measured Fe isotope ratios combined with oxygen isotope and chemical data confirm that the 'Group 4' CS population, composed of ^{16}O-depleted spherules represents an actual Solar System reservoir, and cannot result from the alteration of a known precursor group. These spherules are chondritic in nature but their parent body remains unidentified among larger scale meteorites to date. Also, the combination of Fe and O isotope values shows potential to identify ECs.

By combining the Fe and O isotope ratios with textural information and elemental compositions, the contributions of the various processes leading to chemical and isotope fractionation can be disentangled. This approach represents a significant step forward in our understanding of the effects that take place during atmospheric passage and helps to precisely constrain the nature of micrometeorite parent bodies.

Declaration of Competing Interest

The authors declare that they have no known competing financial interests or personal relationships that could have appeared to influence the work reported in this paper.

ACKNOWLEDGEMENTS

The authors thank Cecile Engrand and the anonymous second reviewer for critically reading the manuscript and providing valuable feedback, which substantially improved the quality of this work. We also thank associate editor, Christian Koeberl, for his aid on this manuscript. SG and PC are supported by the Research Foundation – Flanders (FWO-Vlaanderen), and the VUB strategic program. BS acknowledges the support of the Fonds voor Wetenschappelijk Onderzoek (FWO-Vlaanderen) as part of his PhD Fellowship. SCh acknowledges his postdoctoral grant from FWO-Vlaanderen in the context of an "Excellence of Science (EoS)" project (ET-HoME – ID 30442502). FV, VD, PC and SG also acknowledge support from the EoS project "ET-HoME". SG, VD and PC thank the Belgian Science Policy (BELSPO) for support through different projects (BELAM, Amundsen and BAMM), CGdV acknowledges the grant from Marie Curie Clarin-

COFUND project of the Principality of Asturias and the European Union. FWO-Vlaanderen is also acknowledged for providing the funding for the acquisition of MC-ICP-MS instrumentation (ZW15-02 – G0H6216N). VD thanks the FRS-FNRS for present support. NanoSIMS supported by EuroPlanet 15-EPN-033.

APPENDIX A. SUPPLEMENTARY MATERIAL

Supplementary data to this article can be found online at https://doi.org/10.1016/j.gca.2022.02.008.

REFERENCES

Alexander C. M. O., Taylor S., Delaney J. S., Ma P. and Herzog G. F. (2002) Mass-dependent fractionation of Mg, Si, and Fe isotopes in five stony cosmic spherules. *Geochim. Cosmochim. Acta* **66**, 173–183.

Audi G., Wapstra A. H. and Thibault C. (2003) The Ame 2003 atomic mass evaluation - (II). Tables, graphs and references. *Nucl. Phys. A* **729**, 337–676.

Barrat J. A., Rouxel O., Wang K., Moynier F., Yamaguchi A., Bischoff A. and Langlade J. (2015) Early stages of core segregation recorded by Fe isotopes in an asteroidal mantle. *Earth Planet. Sci. Lett.* **419**, 93–100.

Chernonozhkin S. M., Goderis S., Costas-Rodríguez M., Claeys P. and Vanhaecke F. (2016) Effect of parent body evolution on equilibrium and kinetic isotope fractionation: A combined Ni and Fe isotope study of iron and stony-iron meteorites. *Geochim. Cosmochim. Acta* **186**, 168–188.

Chernonozhkin S. M., González de Vega C., Artemieva N., Soens B., Belza J., Bolea-Fernandez E., Van Ginneken M., Glass B. P., Folco L., Genge M. J., Claeys P. h., Vanhaecke F. and Goderis S. (2021) Isotopic evolution of planetary crusts by hypervelocity impacts evidenced by Fe in microtektites. *Nat. Commun.* **12**(1), 5646.

Clayton R. N. (1993) Oxygen isotopes in meteorites. *Annu. Rev. Earth Planet. Sci.* **21**, 115–149.

Clayton R. N. and Mayeda T. K. (1999) Oxygen isotope studies of carbonaceous chondrites. *Geochim. Cosmochim. Acta* **63**(13–14), 2089–2104.

Clayton R. N., Mayeda T. K. and Brownlee D. E. (1986) Oxygen isotopes in deep-sea spherules. *Earth Planet. Sci. Lett.* **79**, 235–240.

Clayton R. N., Mayeda T. K., Goswami J. N. and Olsen E. J. (1991) Oxygen isotope studies of ordinary chondrites. *Geochim. Cosmochim. Acta* **55**(8), 2317–2337.

Clayton R. N., Onuma N. and Mayeda T. K. (1976) A classification of meteorites based on oxygen isotopes. *Earth Planet. Sci. Lett.* **30**, 10–18.

Cordier C. and Folco L. (2014) Oxygen isotopes in cosmic spherules and the composition of the near Earth interplanetary dust complex. *Geochim. Cosmochim. Acta* **146**, 18–26.

Cordier C., Folco L., Suavet C., Sonzogni C. and Rochette P. (2011a) Major, trace element and oxygen isotope study of glass cosmic spherules of chondritic composition: The record of their source material and atmospheric entry heating. *Geochim. Cosmochim. Acta* **75**, 5203–5218.

Cordier C., Folco L. and Taylor S. (2011b) Vestoid cosmic spherules from the South Pole Water Well and Transantarctic Mountains (Antarctica): A major and trace element study. *Geochim. Cosmochim. Acta* **75**, 1199–1215.

Cordier C., Suavet C., Folco L., Rochette P. and Sonzogni C. (2012) HED-like cosmic spherules from the Transantarctic Mountains, Antarctica: Major and trace element abundances and oxygen isotopic compositions. *Geochim. Cosmochim. Acta* **77**, 515–529.

Craddock P. R., Warren J. M. and Dauphas N. (2013) Abyssal peridotites reveal the near-chondritic Fe isotopic composition of the Earth. *Earth Planet. Sci. Lett.* **365**, 63–76.

Dermott S. F., Durda D., Gustafson B., Jayaraman S., Xu Y. L., Nicholson P. D. and Gomes R. S. (1991) The origin and evolution of the zodiacal dust cloud. In *Asteroids, Comets, Meteors 1991* (eds. A. W. Harris and E. Bowell). Lunar Planet. Inst., Houston, pp. 153–156.

Engrand C., McKeegan K. D. and Leshin L. A. (1999) Oxygen isotopic compositions of individual minerals in Antarctic micrometeorites: Further links to carbonaceous chondrites. *Geochim. Cosmochim. Acta* **63**, 2623–2636.

Engrand C., McKeegan K. D., Leshin L. A., Herzog G. F., Schnabel C., Nyquist L. E. and Brownlee D. E. (2005) Isotopic compositions of oxygen, iron, chromium, and nickel in cosmic spherules: Toward a better comprehension of atmospheric entry heating effects. *Geochim. Cosmochim. Acta* **69**, 5365–5385.

Fischer M. B., Oeser M., Weyer S., Folco L., Peters S. T. M., Zahnow F. and Pack A. (2021) I-Type cosmic spherules as proxy for the Δ′17O of the atmosphere—A calibration with quaternary air. *Paleoceanogr. Paleoclimatol.* **36**(3), e2020PA004159.

Flynn G. J. (1992) Atmospheric entry survival of large micrometeorites: Implications for their sources and for the cometary contribution to the zodiacal cloud. In *Asteroids, Comets, Meteors 1991* (eds. A. W. Harris and E. Bowell). Lunar Planet. Inst., Houston, pp. 195–200.

Flynn G. J. and Sutton S. R. (1992) Trace elements in chondritic stratospheric particles – Zinc depletion as a possible indicator of atmospheric entry heating. In *In Lunar and Planetary Science Conference Proceedings*, pp. 171–184.

Flynn G. J., Durda D. D., Sandel L. E., Kreft J. W. and Strait M. M. (2009) Dust production from the hypervelocity impact disruption of the Murchison hydrous CM2 meteorite: Implications for the disruption of hydrous asteroids and the production of interplanetary dust. *Planet. Space Sci.* **57**, 119–126.

Genge M. J. (2008) Micrometeorites and their implications for meteors. *Earth. Moon. Planets* **102**, 525–535.

Genge M. J., Engrand C., Gounelle M. and Taylor S. (2008) The classification of micrometeorites. *Meteorit. Planet. Sci.* **43**, 497–515.

Genge M. J. and Grady M. M. (1998) Melted micrometeorites from Antarctic ice with evidence for the separation of immiscible Fe-Ni-S liquids during entry heating. *Meteorit. Planet. Sci.* **33**, 425–434.

Goderis S., Chakrabarti R., Debaille V. and Kodolányi J. (2016) Isotopes in cosmochemistry: Recipe for a solar system. *J. Anal. At. Spectrom.* **31**, 841–862.

Goderis S., Soens B., Huber M. S., McKibbin S., van Ginneken M., Van Maldeghem F., Debaille V., Greenwood R. C., Franchi I. A., Cnudde V., Van Malderen S., Vanhaecke F., Koeberl C., Topa D. and Claeys P. (2020) Cosmic spherules from Widerøefjellet, Sør Rondane Mountains (East Antarctica). *Geochim. Cosmochim. Acta* **270**, 112–143.

González de Vega C., Chernonozhkin S. M., Grigoryan R., Costas-Rodríguez M. and Vanhaecke F. (2020a) Characterization of the new isotopic reference materials IRMM-524A and ERM-AE143 for Fe and Mg isotopic analysis of geological and biological samples. *J. Anal. At. Spectrom.* **35**, 2517–2529.

González de Vega C., Costas-Rodríguez M., Van Acker T., Goderis S. and Vanhaecke F. (2020b) Nanosecond laser ablation-multicollector inductively coupled plasma-mass spec-

trometry for in situ Fe isotopic analysis of micrometeorites: Application to micrometer-sized glassy cosmic spherules. *Anal. Chem.* **92**, 3572–3580.

Goodrich C. A. and Delaney J. S. (2000) Fe/Mg–Fe/Mn relations of meteorites and primary heterogeneity of primitive achondrite parent bodies. *Geochim. Cosmochim. Acta* **64**, 149–160.

Greshake A., Kloeck W., Arndt P., Maetz M., Flynn G. J., Bajt S. and Bischoff A. (1998) Heating experiments simulating atmospheric entry heating of micrometeorites: Clues to their parent body sources. *Meteorit. Planet. Sci.* **33**, 267–290.

Gussone N., Eisenhauer A., Heuser A., Dietzel M., Bock B., Böhm F., Spero H. J., Lea D. W., Bijma J. and Nägler T. F. (2003) Model for kinetic effects on calcium isotope fractionation (δ^{44}Ca) in inorganic aragonite and cultured planktonic foraminifera. *Geochim. Cosmochim. Acta* **67**, 1375–1382.

Herzog G. F., Xue S., Hall G. S., Nyquist L. E., Shih C. Y., Wiesmann H. and Brownlee D. E. (1999) Isotopic and elemental composition of iron, nickel, and chromium in type I deep-sea spherules: Implications for origin and composition of the parent micrometeoroids. *Geochim. Cosmochim. Acta* **63**, 1443–1457.

Huang F., Chakraborty P., Lundstrom C. C., Holmden C., Glessner J. J. G., Kieffer S. W. and Lesher C. E. (2010) Isotope fractionation in silicate melts by thermal diffusion. *Nature* **464**, 396–400.

Kral Q., Krivov A. V., Defrère D., van Lieshout R., Bonsor A., Augereau J.-C., Thébault P., Ertel S., Lebreton J. and Absil O. (2017) Exozodiacal clouds: Hot and warm dust around main sequence stars. *Astron. Rev.* **13**, 69–111.

Lesher C. E. and Walker D. (1986) Solution properties of silicate liquids from thermal diffusion experiments. *Geochim. Cosmochim. Acta* **50**, 1397–1411.

Lodders K. (2003) Solar system abundances and condensation temperatures of the elements. *Astrophys. J.* **591**, 1220–1247.

Love S. and Brownlee D. E. (1991) Heating and thermal transformation of micrometeoroids entering the Earth's atmosphere. *Icarus* **89**, 26–43.

Love S. G. and Brownlee D. E. (1993) A direct measurement of the terrestrial mass accretion rate of cosmic dust. *Science* **262**, 550–553.

Ludwig K. R. (2008) User's Manual for Isoplot 3.70. Berkeley Geochronol. Cent. Spec. Publ..

Van Malderen S. J. M., Van Acker T. and Vanhaecke F. (2020) Sub-micrometer nanosecond LA-ICP-MS imaging at pixel acquisition rates above 250 Hz via a low-dispersion setup. *Anal. Chem.* **92**, 5756–5764.

Nesvorný D., Jenniskens P., Levison H. F., Bottke W. F., Vokrouhlický D. and Gounelle M. (2010) Cometary origin of the zodiacal cloud and carbonaceous micrometeorites. Implications for hot debris disks. *Astrophys. J.* **713**, 816–836.

Newton J., Franchi I. A. and Pillinger C. T. (2010) The oxygen-isotopic record in enstatite meteorites. *Meteorit. Planet. Sci.* **35** (4), 689–698.

Pack A., Höweling A., Hezel D. C., Stefanak M. T., Beck A.-K., Peters S. T. M., Sengupta S., Herwartz D. and Folco L. (2017) Tracing the oxygen isotope composition of the upper Earth's atmosphere using cosmic spherules. *Nat. Commun.* **8**, 15702.

Plane J. M. C., Flynn G. J., Määttänen A., Moores J. E., Poppe A. R., Carrillo-Sanchez J. D. and Listowski C. (2018) Impacts of cosmic dust on planetary atmospheres and surfaces. *Space Sci. Rev.* **214**(1), 23.

Presper T., Kurat G., Koeberl C., Palme H. and Maurette M. (1993) Elemental depletions in Antarctic micrometeorites and Arctic cosmic spherules: Comparison and relationships. *In Lunar and Planetary Science Conference*.

Richter F. M. (2011) Isotope fractionation in silicate melts by thermal diffusion. *Nature* **472**, 396–400.

Richter F. M., Dauphas N. and Teng F. Z. (2009a) Non-traditional fractionation of non-traditional isotopes: Evaporation, chemical diffusion and Soret diffusion. *Chem. Geol.* **258**, 92–103.

Richter F. M., Watson E. B., Mendybaev R. A., Teng F. Z. and Janney P. E. (2008) Magnesium isotope fractionation in silicate melts by chemical and thermal diffusion. *Geochim. Cosmochim. Acta* **72**, 206–220.

Richter F. M., Watson E. B., Mendybaev R., Dauphas N., Georg B., Watkins J. and Valley J. (2009b) Isotopic fractionation of the major elements of molten basalt by chemical and thermal diffusion. *Geochim. Cosmochim. Acta* **73**, 4250–4263.

Rochette P., Folco L., Suavet C., Van Ginneken M., Gattacceca J., Perchiazzi N., Braucher R. and Harvey R. P. (2008) Micrometeorites from the transantarctic mountains. *Proc. Natl. Acad. Sci.* **105**, 18206–18211.

Rock N. M. S. and Duffy T. R. (1986) REGRES: A FORTRAN-77 program to calculate nonparametric and "structural" parametric solutions to bivariate regression equations. *Comput. Geosci.* **12**, 807–818.

Rojas J., Duprat J., Engrand C., Dartois E., Delauche L., Godard M., Gounelle M., Carrillo-Sánchez J. D., Pokorný P. and Plane J. M. C. (2021) The micrometeorite flux at Dome C (Antarctica), monitoring the accretion of extraterrestrial dust on Earth. *Earth Planet. Sci. Lett.* **560**, 116794.

Rubin A. E. and Grossman J. N. (2010) Meteorite and meteoroid: New comprehensive definitions. *Meteorit. Planet. Sci.* **45**, 114–122.

Rudraswami N. G., Genge M. J., Marrocchi Y., Villeneuve J. and Taylor S. (2020) The oxygen isotope compositions of large numbers of small cosmic spherules: Implications for their sources and the isotopic composition of the upper atmosphere. *J. Geophys. Res. Planets* **125**(10), e2020JE006414.

Rudraswami N. G., Shyam P. M., Babu E. V. S. S. K., Vijaya K. T., Feng W. and Plane J. M. C. (2012) Fractionation and fragmentation of glass cosmic spherules during atmospheric entry. *Geochim. Cosmochim. Acta* **99**, 110–127.

Rumble D., Miller M. F., Franchi I. A. and Greenwood R. C. (2007) Oxygen three-isotope fractionation lines in terrestrial silicate minerals: An inter-laboratory comparison of hydrothermal quartz and eclogitic garnet. *Geochim. Cosmochim. Acta* **71**, 3592–3600.

Schauble E. A. (2007) Role of nuclear volume in driving equilibrium stable isotope fractionation of mercury, thallium, and other very heavy elements. *Geochim. Cosmochim. Acta* **71**, 2170–2189.

Soens B., Suttle M. D., Maeda R., Vanhaecke F., Yamaguchi A., Van Ginneken M., Debaille V., Claeys P. and Goderis S. (2020) Evidence for the presence of chondrule- and CAI-derived material in an isotopically anomalous Antarctic micrometeorite. *Meteorit. Planet. Sci.* **55**, 2703–2726.

Starkey N. A. and Franchi I. A. (2013) Insight into the silicate and organic reservoirs of the comet forming region. *Geochim. Cosmochim. Acta* **105**, 73–91.

Suavet C., Alexandre A., Franchi I. A., Gattacceca J., Sonzogni C., Greenwood R. C., Folco L. and Rochette P. (2010) Identification of the parent bodies of micrometeorites with high-precision oxygen isotope ratios. *Earth Planet. Sci. Lett.* **293**, 313–320.

Suttle M. D., Dionnet Z., Franchi I., Folco L., Gibson J., Greenwood R. C., Rotundi A., King A. and Russell S. S. (2020) Isotopic and textural analysis of giant unmelted micrometeorites – identification of new material from intensely altered ^{16}O-poor water-rich asteroids. *Earth Planet. Sci. Lett.* **546**, 116444.

Taylor S., Alexander C. M. O'. D., Delaney J., Ma P., Herzog G. F. and Engrand C. (2005) Isotopic fractionation of iron, potassium, and oxygen in stony cosmic spherules: Implications for heating histories and sources. *Geochim. Cosmochim. Acta* **69**, 2647–2662.

Taylor S. and Brownlee D. E. (1991) Cosmic spherules in the geologic record. *Meteorit. Planet. Sci.* **26**, 203–211.

Taylor S., Herzog G. F. and Delaney J. S. (2007) Crumbs from the crust of Vesta: Achondritic cosmic spherules from the South Pole water well. *Meteorit. Planet. Sci.* **42**, 223–233.

Taylor S., Lever J. H. and Harvey R. P. (2000) Numbers, types, and compositions of an unbiased collection of cosmic spherules. *Meteorit. Planet. Sci.* **35**, 651–666.

Theil H. (1992) A rank-invariant method of linear and polynomial regression analysis. In *Henri Theil's Contributions to Economics and Econometrics* (eds. B. Raj and J. Koerts). Springer, Dordrecht, pp. 345–381.

Thiemens M. H., Heidenreich J. E., Zipf E. C., Erdman P. W. and van Egmond C. (1983) The mass-independent fractionation of oxygen: A novel isotope effect and its possible cosmochemical implications. *Science* **219**, 1073–1075.

Thiemens M. H., Jackson T., Zipf E. C., Erdman P. W. and van Egmond C. (1995) Carbon dioxide and oxygen isotope anomalies in the mesosphere and stratosphere. *Science* **270**, 969–972.

Toppani A., Libourel G., Engrand C. and Maurette M. (2001) Experimental simulation of atmospheric entry of micrometeorites. *Meteorit. Planet. Sci.* **36**, 1377–1396.

van Ginneken M., Gattacceca J., Rochette P., Sonzogni C., Alexandre A., Vidal V. and Genge M. J. (2017) The parent body controls on cosmic spherule texture: Evidence from the oxygen isotopic compositions of large micrometeorites. *Geochim. Cosmochim. Acta* **212**, 196–210.

van Ginneken M., Genge M. J., Folco L. and Harvey R. P. (2016) The weathering of micrometeorites from the Transantarctic Mountains. *Geochim. Cosmochim. Acta* **179**, 1–31.

Vermeesch P. (2018) IsoplotR: A free and open toolbox for geochronology. *Geosci. Front.* **9**, 1479–1493.

Vugrinovich R. G. (1981) A distribution-free alternative to least-squares regression and its application to Rb/Sr isochron calculations. *J. Int. Assoc. Math. Geol.* **13**, 443–454.

Wang J., Davis A. M., Clayton R. N. and Mayeda T. K. (1994) Kinetic isotopic fractionation during the evaporation of the iron oxide from liquid state. *In Lunar and Planetary Science Conference* Proceedings, (25), 1459–1460.

Wombacher F. and Rehkämper M. (2003) Investigation of the mass discrimination of multiple collector ICP-MS using neodymium isotopes and the generalised power law. *J. Anal. At. Spectrom.* **18**, 1371–1375.

Wyatt S. P. and Whipple F. L. (1950) The Poynting-Robertson effect on meteor orbits. *Astrophys. J.* **111**, 134–141.

Yada T., Nakamura T., Noguchi T., Matsumoto N., Kusakabe M., Hiyagon H., Ushikubo T., Sugiura N., Kojima H. and Takaoka N. (2005) Oxygen isotopic and chemical compositions of cosmic spherules collected from the Antarctic ice sheet: Implications for their precursor materials. *Geochim. Cosmochim. Acta* **69**, 5789–5804.

York D., Evensen N. M., Martı´nez M. L. and De Basabe Delgado J. (2004) Unified equations for the slope, intercept, and standard errors of the best straight line. *Am. J. Phys.* **72**, 367–375.

Young E. D., Galy A. and Nagahara H. (2002) Kinetic and equilibrium mass-dependent isotope fractionation laws in nature and their geochemical and cosmochemical significance. *Geochim. Cosmochim. Acta* **66**, 1095–1104.

Zolensky M., Bland P., Brown P. and Halliday I. (2006) Flux of extraterrestrial materials. In *Meteorites and the Early Solar System II* (eds. D. S. Lauretta and H. Y. McSween). University of Arizona Press, Arizona, pp. 869–888.

Associate editor: Christian Koeberl